REPORT DOCUMENTATION PAGE

Form Approved OMB NO. 0704-0188

1. REPORT DATE (DD-MM-YYYY)	2. REPORT TYPE	3. DATES COVERED (From - To)
	New Reprint	-

4. TITLE AND SUBTITLE

Recent developments in the photophysics of single-walled carbon nanotubes for their use as active and passive material elements in thin film photovoltaics

5a. CONTRACT NUMBER
W911NF-12-1-0025

5b. GRANT NUMBER

5c. PROGRAM ELEMENT NUMBER
611103

6. AUTHORS

Michael S. Arnold, Jeffrey L. Blackburn, Jared J. Crochet, Stephen K. Doorn, Juan G. Duque, Aditya Mohite, Hagen Telg

5d. PROJECT NUMBER

5e. TASK NUMBER

5f. WORK UNIT NUMBER

7. PERFORMING ORGANIZATION NAMES AND ADDRESSES

University of Wisconsin - Madison
The Board of Regents of the University of Wisconsin System
Suite 6401
Madison, WI 53715 -1218

8. PERFORMING ORGANIZATION REPORT NUMBER

9. SPONSORING/MONITORING AGENCY NAME(S) AND ADDRESS(ES)

U.S. Army Research Office
P.O. Box 12211
Research Triangle Park, NC 27709-2211

10. SPONSOR/MONITOR'S ACRONYM(S)
ARO

11. SPONSOR/MONITOR'S REPORT NUMBER(S)
58398-EL-PCS.3

12. DISTRIBUTION AVAILIBILITY STATEMENT

Approved for public release; distribution is unlimited.

13. SUPPLEMENTARY NOTES

The views, opinions and/or findings contained in this report are those of the author(s) and should not contrued as an official Department of the Army position, policy or decision, unless so designated by other documentation.

14. ABSTRACT

The search for environmentally clean energy sources has spawned a wave of research into the use of carbon nanomaterials for photovoltaic applications. In particular, research using semiconducting single-walled carbon nanotubes has undergone dramatic transformations due to the availability of high quality samples through colloidal separation techniques. This has led to breakthrough discoveries on how energy and charge transport occurs in these materials and points to applications in energy harvesting. We present a review of the relevant photophysics of

15. SUBJECT TERMS

Carbon nanotube photovoltaic photophysics solar cell perspective

16. SECURITY CLASSIFICATION OF:			17. LIMITATION OF ABSTRACT	15. NUMBER OF PAGES	19a. NAME OF RESPONSIBLE PERSON
a. REPORT	b. ABSTRACT	c. THIS PAGE			Michael Arnold
UU	UU	UU	UU		19b. TELEPHONE NUMBER 608-262-3863

Report Title

Recent developments in the photophysics of single-walled carbon nanotubes for their use as active and passive material elements in thin film photovoltaics

ABSTRACT

The search for environmentally clean energy sources has spawned a wave of research into the use of carbon nanomaterials for photovoltaic applications. In particular, research using semiconducting single-walled carbon nanotubes has undergone dramatic transformations due to the availability of high quality samples through colloidal separation techniques. This has led to breakthrough discoveries on how energy and charge transport occurs in these materials and points to applications in energy harvesting. We present a review of the relevant photophysics of carbon nanotubes that dictate processes important for integration as active and passive material elements in thin film photovoltaics. Fundamental processes ranging from light absorption and internal conversion to exciton transport and dissociation are discussed in detail from both a spectroscopic and a device perspective. We also give a perspective on the future of these fascinating materials to be used as active and passive material elements in photovoltaics.

REPORT DOCUMENTATION PAGE (SF298)
(Continuation Sheet)

Continuation for Block 13

ARO Report Number 58398.3-EL-PCS
Recent developments in the photophysics of sin ...

Block 13: Supplementary Note

Approved for public release; distribution is unlimited.

PCCP

RSC Publishing

PERSPECTIVE

View Article Online
View Journal | View Issue

Cite this: *Phys. Chem. Chem. Phys.*, 2013, **15**, 14896

Recent developments in the photophysics of single-walled carbon nanotubes for their use as active and passive material elements in thin film photovoltaics

Michael S. Arnold,[ab] Jeffrey L. Blackburn,[c] Jared J. Crochet,*[d] Stephen K. Doorn,[e] Juan G. Duque,[d] Aditya Mohite[e] and Hagen Telg[e]

Received 9th May 2013,
Accepted 4th July 2013

DOI: 10.1039/c3cp52752b

www.rsc.org/pccp

The search for environmentally clean energy sources has spawned a wave of research into the use of carbon nanomaterials for photovoltaic applications. In particular, research using semiconducting single-walled carbon nanotubes has undergone dramatic transformations due to the availability of high quality samples through colloidal separation techniques. This has led to breakthrough discoveries on how energy and charge transport occurs in these materials and points to applications in energy harvesting. We present a review of the relevant photophysics of carbon nanotubes that dictate processes important for integration as active and passive material elements in thin film photovoltaics. Fundamental processes ranging from light absorption and internal conversion to exciton transport and dissociation are discussed in detail from both a spectroscopic and a device perspective. We also give a perspective on the future of these fascinating materials to be used as active and passive material elements in photovoltaics.

1 Introduction

The development of energy sources that will satisfy the world's growing energy demand has been identified as the single greatest science challenge of the 21st century. Furthermore, the consequences for national security and global climate of a continuing reliance on fossil fuels are a cause for growing concern. The ability to address this challenge, of securing sufficient energy resources and decreasing the dependence on fossil fuels, remains at the forefront of energy research and policy interest. While other carbon-free or carbon-neutral energy sources (*e.g.* nuclear, geothermal, biomass) will likely contribute to the future energy mix, solar energy has the greatest long-term potential to address this need.

Carbon nanotubes are versatile materials that offer tantalizing possibilities for increasing the efficiency and functionality of next-generation solar cells. Widely tunable properties open up possibilities for using nanotubes in many different roles in photovoltaics (PV). Nanotubes are either metallic or semiconducting depending on their physical structure, which is defined by two integer indices (n,m) that specify how a nanotube is rolled up into a seamless cylinder from a sheet of graphene.[1] The bandgap and optical properties of semiconducting nanotubes are widely tunable with the nanotube diameter, enabling either the selective or broadband absorption of light spanning from the ultraviolet to the near-infrared.[2] The electrical and optical properties of semiconducting carbon nanotube species can be additionally tailored by doping[3] or by controllably coupling nanotubes to one-another in hexagonally packed aggregates called bundles, which also allow for tailoring of their photoexcited electrical response.[4,5]

The different species of nanotubes lend themselves to distinct applications. Films of metallic and doped semiconducting nanotubes are leading candidates to replace conducting oxides as the transparent contacts of both inorganic and organic solar cells because of the nanotubes' excellent mechanical flexibility and high conductivity. Semiconducting carbon nanotubes are appealing materials for enhancing charge separation and collection from light absorbing semiconducting polymers and dyes in organic solar cells[6–10] because of their wire-like geometry and ultrafast charge transport mobility ($\sim 10^4$ cm^2 V^{-1} s^{-1}).[11,12] Finally, most recently it has been realized that semiconducting nanotubes themselves are highly attractive as the active, light-absorbing components of solar cells because of their strong dye-like optical absorptivity and tunable spectral response.[2,13–16] Entirely new classes of high-efficiency and photostable

[a] *Materials Science Program, University of Wisconsin, Madison, Wisconsin, USA*
[b] *Department of Materials Science and Engineering, University of Wisconsin, Madison, Wisconsin, USA*
[c] *National Renewable Energy Laboratory, Golden, Colorado, USA*
[d] *Physical Chemistry and Applied Spectroscopy, Los Alamos National Laboratory, New Mexico, USA. E-mail: jcrochet@lanl.gov*
[e] *Center for Integrated Nanotechnologies, Los Alamos National Laboratory, New Mexico, USA*

single- and multi-junction solar cells are envisioned based on type-II donor–acceptor heterojunctions between nanotube photoabsorbers and complementary semiconductors[7,17–25] or even solely between different (n,m) nanotube species.[5]

Overall, the exploration of carbon nanotubes in solar cells is still in its genesis. One reason is that it has only recently become possible to isolate nanotubes by their electronic-type (metallic *versus* semiconducting), bandgap, diameter, and chirality with sufficient yield and purity to exploit the intrinsic properties of the different types of nanotubes.[18,26–35] Furthermore, we have just recently begun to understand the intricacies of the photophysical responses and behaviors of these materials[5,16,36–52] in enough detail to utilize them in light harvesting applications. The rapid advances in the science and technology of carbon nanotubes have now made it possible to explore these exceptional next-generation materials for solar cell applications and many opportunities remain to be discovered. Here, we review prominent developments in the understanding of the photophysics of carbon nanotubes and their use in thin-film photovoltaics and offer a perspective on the future of exploiting carbon nanotubes in solar cells, focusing in particular on the roles of nanotubes such as: (i) transparent conductors, (ii) charge collectors, (iii) photoabsorbers, and (iv) charge generators.

2 Physical structure

Visualization of the side wall of a single-walled carbon nanotube (SWNT) makes the similarity of the atomic structures of nanotubes and graphene obvious; a nanotube represents a sheet of graphene which is rolled up into a seamless cylinder, Fig. 1. In this picture, the initial sheet of graphene is a rectangle where the side along which it is rolled up, given by the chiral vector $\vec{c}_h$ (eqn (1)) must be a multiple of the graphene lattice vectors $\vec{a}_1$ and $\vec{a}_2$,

$$\vec{c}_h = n\vec{a}_1 + m\vec{a}_2, \quad (1)$$

such that the coefficients (n,m) define the tube circumference $L = a_0\sqrt{n^2 + m^2 + nm}$ where a_0 is the length of the graphene primitive lattice vectors. The atomic structure of a nanotube is, except for its length, entirely described by eqn (1). Thus, carbon nanotubes are referred to in short-hand by their chiral indices, n and m: *i.e.* (n,m).

Many of the basic physical properties of carbon nanotubes strongly vary for different (n,m) indices. For example, the electronic character can vary from metallic to semiconducting with direct bandgaps ranging from 0.1 to 1.5 eV. Further examples of strong variations for different (n,m) have been observed in optical absorption strengths[53,54] and electron–phonon coupling strengths.[55–58] These two particular intrinsic physical properties underlie many other phenomena related to optics and transport which in turn can be expected to show strong chirality variations.

Since many proposed applications of carbon nanotubes depend on particular properties provided only by a single (n,m) or a subset of tubes it is essential to have characterization techniques which are able to assign the chiral indices. To date there exist four main techniques to perform (n,m) assignment: photoluminescence excitation spectroscopy (PLE),[14] resonant Raman spectroscopy (RRS),[59–63] electron diffraction,[64] and scanning tunneling microscopy.[65] While the latter two techniques are experimentally very challenging and suitable only for single tube assignments, the first two can be conducted on relatively simple experimental setups and both on individual tubes and nanotube ensembles.[66,67] The advantage of PLE over RRS is that one can probe the existence of all semiconducting species in a sample in a relatively short time. On the other hand, RRS is able to perform assignments of metallic and bundled tubes, both of which give no or very weak luminescence signal.

Both techniques, PLE and RRS, take advantage of the series of well defined optical transitions in each nanotube that act as a fingerprint for each particular (n,m) index. However, knowing only one transition energy is not sufficient to perform an assignment. In the case of PLE the assignment is achieved by correlating the second with the first optical transition. Raman based assignments take advantage of many Raman modes being diameter dependent. As we show in the following section, the correlation of the diameter and the transition energies leads to a characteristic pattern. Therefore any experiment which correlates one optical transition and the tube diameter can be used for a (n,m) assignment.[62,63]

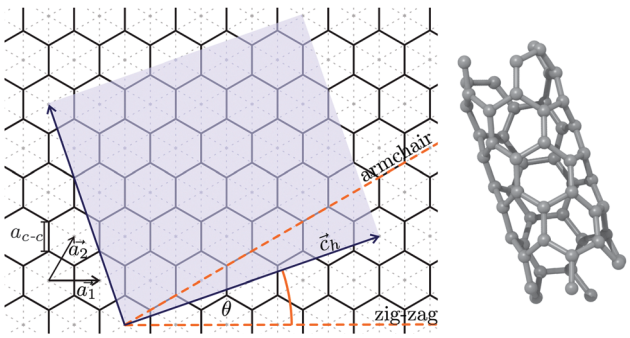

Fig. 1 Lattice structure of graphene with basis vectors $\vec{a}_1 = (1,0)\cdot a_0$ and $\vec{a}_2 = (0.5, 0.5\sqrt{3})\cdot a_0$ (a_0 is the length of the graphene primitive lattice vectors); $a_0 = \sqrt{3}\cdot a_{c-c}$ with a_{c-c} being the distance between neighboring carbon atoms. Rolling up the highlighted area to a cylinder along the vector $\vec{c}_h$ forms the unit cell of a (4,2) tube.

3 Electronic structure

Unlike molecules whose molecular orbitals are localized amongst the atoms with discrete quantum numbers, in condensed matter systems such as carbon nanotubes the wavefunctions are delocalized and quantum numbers are continuous as a wavevector k within a certain angular momentum state μ. Therefore, the simplest way to approximate the electronic structure, and therefore the optical transition energies of a particular carbon nanotube, is by performing a zone-folding on the band-structure of an infinitely delocalized π conjugated system: graphene. In Fig. 2 we show the valence, π, bands and the conduction, π*, bands of graphene as a two-dimensional

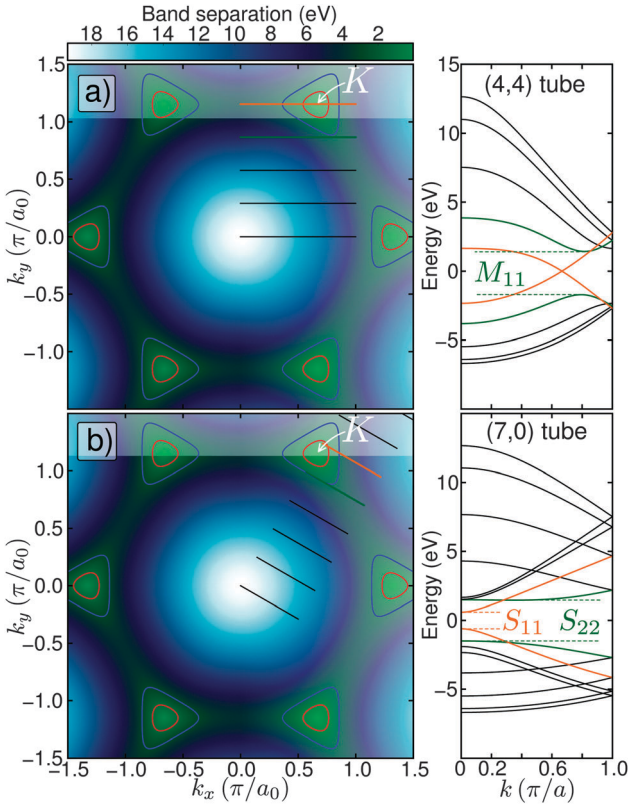

Fig. 2 Lines of allowed states (LOAS) for (a) the (4,4) armchair tube and (b) the (7,0) zig-zag tube both plotted on a contour plot of the electronic band structure of graphene. The red and blue contour lines around the *K* point labeled in white illustrate the regime where the band separation is in the visible. (right) Band structure for the particular tube resulting from the graphene band structure along the LOAS. The crossing of the valence and the conduction bands in the case of the (4,4) tube results in a metallic nanotube. The bands of the (7,0) do not cross, which makes it a semiconducting tube. We labeled first and second optical transitions S_{11}, M_{11} and S_{22}, respectively. Here S stands for semiconducting and M for metallic.

projected surface. Note that both bands cross at the Fermi level in the *K* points, which makes graphene a semi-metal. Regarding nanotubes, we have an extended (infinitely large) system with a translational symmetry solely along the tube axis. Therefore we can assume a continuum of allowed wave vectors $\vec{k}$ solely along this direction. Waves which travel along the circumference $\vec{c}_h$ of the tube interfere destructively unless they fulfill the periodic boundary condition,

$$\vec{c}_h \cdot \vec{k} = 2\pi\mu, \qquad (2)$$

where μ is the circumferential quantum number.

This leaves the *k*-space of graphene with lines of allowed states with an energetic spacing dependent on $|\vec{c}_h|$, and thus on the diameter *d* of the particular tube, $|\Delta\vec{k}| = 2/d$. The length of the lines with respect to the Brillouin zone is given by the inverse length of the nanotube unit cell *a*, $T_r = \pi/a$. On the left of Fig. 1 we show the lines of allowed $\vec{k}$ plotted on top of a contour plot of the band-structure of graphene. The actual band-structure of the particular tube, shown on the right of Fig. 2, is given by the band-structure of graphene along the lines.

In the case of the (4,4) tube the zone folding results in a zero bandgap, while the band structure of the (7,0) tube reveals a band gap. Note that the diameters of the two tubes are almost the same (0.543 and 0.548 nm). Whether a nanotube is metallic or semiconducting depends solely on whether the graphene *K*-point is among the allowed $\vec{k}$ or not. It can be shown that one third of all (*n*,*m*) result in metallic nanotubes while all others are semiconducting with various band gaps. Optical transitions involving light polarized parallel to the tube axis are given by the separation of the conduction and valence band with the same angular quantum number μ.

A common way to plot the optical transitions of a large variety of (*n*,*m*) is as a function of the tube diameter. Fig. 3 shows such a plot, which is also referred to as the Kataura plot, and which reveals a characteristic pattern of bands (S_1, S_2, M_1,...) and branches (dashed lines, labeled 16–33 in Fig. 3).[68] The bands, which have a $\approx 1/d$ dependence, are related to the different optical transitions in semiconducting and metallic tubes. The branches, which are bending away from the center of the bands, contain tubes with the same band index = $2n + m$ with *m* being the smallest at the small diameter end of the branch, *e.g.* = 19 ⇒ (9,1), (8,3), (7,5).

A weakness of the zone folding approximation described above is the fact that it neglects the curvature of the tube walls and many-body effects which are enhanced by the confinement to 1D. The curvature of the wall and the associated re-hybridization of sp^2 to sp^3 orbitals can be addressed by a symmetry-adapted non-orthogonal tight-binding model.[69] However, to account for electron–electron or even electron–hole interactions, sophisticated calculations are necessary, which can only be conducted on a small subset of (*n*,*m*) with a sufficiently small unit cell.[70–72] It has been shown by calculations and experiment that the electron–hole interaction in nanotubes is strong and excited states can no longer be described by a free particle picture as in graphene but by a

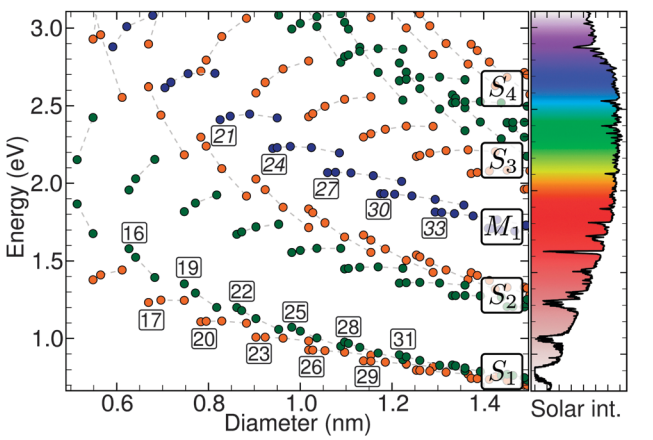

Fig. 3 Kataura plot: optical transition energies of carbon nanotubes as a function of tube diameter. Plot includes the first four optical transitions of semiconducting tubes, S_{11}, S_{22}, S_{33}, and S_{44} and the first optical transition M_{11} of metallic nanotubes. The diameter range covers the diameter distribution of the most common types of single walled carbon nanotubes. The ground observed solar spectrum is given to the right.

bound excitonic state.[37,73–75] Note that many properties, particularly trends like diameter or chiral angle dependences, can still be predicted on the basis of the less accurate tight-binding description. The Kataura plot for example undergoes merely a distortion along the energy axis when the more accurate approximations are used. The pattern, however, remains the same.

The spectral coverage that can be realized by a particular mixture of nanotubes can be predicted from published measurements[2] of how the transition energies shift as a function of (n,m) and diameter, Fig. 3 (left). It can be seen from Fig. 3 (right) that a combination of nanotubes ranging from 0.6–1.6 nm in diameter is capable of covering the majority of the solar spectrum from $\lambda \approx$ 400–2000 nm. Most single-junction solar cells, however, are designed to capture a narrower spectrum at larger photon energies. Along these lines, a distribution of nanotubes ranging from 0.65–1.0 nm in diameter (with corresponding S_1 optical bandgaps ranging from 1.1–1.4 eV) could be employed to capture photons of energy $h\nu > 1.1$ eV, which is the same spectral range captured by a silicon solar cell. The thermodynamic limit for the efficiency of a solar cell made from these nanotubes would be 30%, close to the Shockley–Queisser limit for a single-junction cell.[18]

3.1 Excitonic effects

Excitonic effects in low-dimensional structures, such as carbon nanotubes, are significant and require theoretical examination beyond the independent particle picture. Moreover, their dynamics and energetics are central to development of active elements in excitonic solar-cells. The most accurate way to treat the electron–hole interaction is by solving the center of mass momentum $2q = k_e + k_h$ dependent Bethe–Salpeter equation (BSE), which determines the correlation functions (envelope of the exciton wavefunction), $A_{v,c,q}$, between valence ($|v,k\rangle$) band electrons and conduction ($|c,k\rangle$) band holes under the influence of the Coulomb potential $V^{c,v}_{k,k'}$. The eigenvalues of the BSE Hamiltonian give the excitation energy in terms of a dispersion relation $\Omega^S(q)$ of each excitonic state.[53,76] The imaginary part of the dielectric function (absorption spectrum) is then calculated with $A_{v,c,q}$ and $\Omega(q)$ where the oscillator strength of a transition is given by $|A_{v,c,q}\langle c,k|\hat{d}|v,k'\rangle|^2$ where $\hat{d}$ is the dipole operator. In principle one could then calculate the excitonic contributions and the free particle contributions to the imaginary part of the dielectric function with and without the e–h interaction. However, due to the reduced screening in one-dimensional systems it turns out that almost all of the oscillator strength is transferred to strongly bound excitons and there is very little absorption from the continuum.[77] Recently it has been shown that upon aggregation the free carrier response can be enhanced, which has implications for carbon nanotube networks as active elements in photovoltaics.[5,78]

It has been predicted[70–72] and shown experimentally[37,73,74,79] that binding energies of excitons in semiconducting SWNTs can range from 0.3–1.0 eV. Some of this large variation can be accounted for by including screening effects of the local dielectric environment.[80] These rather large binding energies give rise to exciton sizes in semiconducting nanotubes (full width half maximum of the nearly Gaussian envelope function[76]) of a few nanometers,[81] which puts excitons in single-walled carbon nanotubes in a class of their own. For example, Wannier–Mott excitons are typically weakly bound (a few tens of meV) and large in size compared to the material lattice constant. In contrast, Frenkel excitons are on the order of the lattice constant of the material and tightly bound (hundreds of meV to an eV). Excitons in semiconducting carbon nanotubes are somewhat of a mixture of these two limiting cases. Interestingly excitonic effects are also important in metallic tubes[73–75] although the binding energy is significantly less, putting them more in the Wannier–Mott class.[79,82]

The fine structure of exciton states is determined by the Coulomb interaction and is deeply rooted in the symmetry of the wavefunctions.[83] The degeneracy of the free particle states arising from the K and K' valleys of the graphene sheet is lifted by the Coulomb interaction due to intra-valley and inter-valley Coulomb mixing. Inter-valley interactions mix electrons from K with holes from K' and *vice versa* and lead to a pair of energetically degenerate states with non-zero center of mass momentum, so called K momentum or $E_\pm$ line group symmetry excitons.[84,85] These states are optically forbidden, but become weakly allowed as vibronic peaks associated with the disorder or D mode[86] arising from longitudinal optical phonons near the K point.[87] Intra-valley interactions give rise to states whose wavefunctions are given by symmetric (bonding) and antisymmetric (anti-bonding) combinations of electron–hole wavefunctions from K and K', see Fig. 4a. The anti-bonding state (antisymmetric), A_1 line group symmetry, is optically allowed by symmetry (from here on labeled S_1 as the first optically allowed singlet exciton) and the bonding state (symmetric), A_2 line group symmetry, is optically forbidden by symmetry.

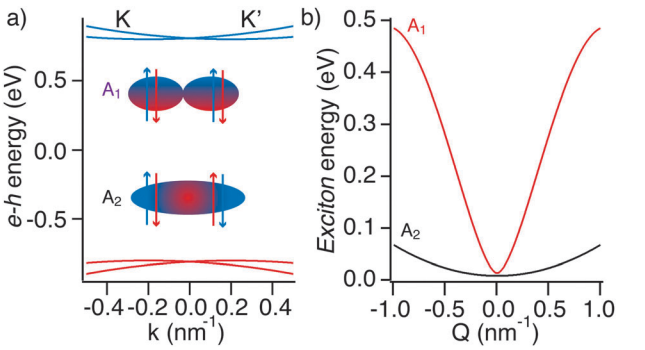

Fig. 4 (a) Free electron–hole dispersion for the lowest band E_{11}, where electrons are in blue and holes are in red. The K/K' valley degeneracy is lifted by the intra-valley electron–hole Coulomb interaction which gives rise to two spin singlet excitons of the possible sixteen excitons that can be made from the K and K' valleys. The configuration of the spin singlets are shown schematically in between the bands. The A_1 exciton is optically allowed and is an anti-bonding configuration of electron–hole pair states from the K and K' valleys. The A_2 exciton is optically forbidden and is a bonding configuration of electron–hole pair states from the K and K' valleys. (b) Exciton dispersions for the bright (purple line) and dark (black line) excitons in (a). The bright exciton has an anomalous dispersion that scales as $Q^2\log(Q^{-1})$ that gives rise to unique transport properties.

These two states (A_1 and A_2) are split by the exchange energy which vanishes for the dark exciton.

Another important quantity that is obtained from the Bethe–Salpeter equation is the exciton dispersion $\varepsilon_{b,q}$, which dictates transport properties through the group velocity: $v_g = \hbar^{-1}\frac{\partial \varepsilon_{b,q}}{\partial q}$. Exciton transport is a key parameter in photovoltaic device performance when bi-layer or bulk heterojunctions are used for dissociating excitons. The S_1 exciton dispersion in carbon nanotubes is non-parabolic because of the exchange interaction and varies as $\varepsilon_{b,q} = \alpha q^2 \log(q_0/|q|)$, where q_0 is a momentum cutoff, q is the center of mass momentum, and α is a coupling constant that measures the strength of the exchange energy.[53,88] Here $\varepsilon_{b,q}$ is singular at $q = 0$, however the singularity is removable as $\lim_{q\to 0}\varepsilon_{b,q} = 0$. Recently this behavior has been explained in terms of the spin–charge velocity separation aspect of the Luttinger liquid,[89] and has roots in the quasi-particle renormalization of the graphene dispersion which does not exactly cancel in one-dimension.[90] From the predictions of Jiang *et al.*[53] for the (6,5) tube, $\alpha = 2.85$ eV nm^2 and $q_0 = 1.4$ nm^{-1}. The dark A_2 exciton, however, has a dispersion of a free particle, $\varepsilon_{d,q} = \hbar^2 q^2/2m^*$, with an effective mass given by $m^* \approx 1.5(m_e^* + m_h^*)$,[88] where $m_e^* + m_h^* = 0.29m_e$ (ref. 91) and * denotes the effective mass and m_e is the bare electron mass, shown in Fig. 4b.

When spin multiplicity (singlets S and triplets T) is considered there is a sixteen-fold degeneracy due to the four spatial combinations of e–h wavefunctions mentioned above and the four possibilities of spin configuration: $S_{\uparrow\downarrow}$ and $T_{\uparrow\uparrow,\downarrow\downarrow,\uparrow\downarrow}$. The energetic ordering of the two singlet states A_1 and A_2 is shown in Fig. 5, and the lowest state in the singlet manifold is A_2 and the next highest is the dipole allowed state A_1 which is $\approx$5 meV higher in energy. The splitting of these two states is given by twice the exchange energy at $Q = 0$, $\Delta \approx 5$ meV,[53,78,92,93] and scattering between the two states is apparently very weak.[94–96]

In the case of the triplets, the exchange interaction vanishes and the ordering is purely due to the direct part of the Coulomb interaction. Interestingly, an accidental degeneracy occurs between the lowest energy singlet exciton, A_2, and its triplet counterpart. This is due to the fundamental symmetry of the wavefunction and how the exchange interaction vanishes in the lowest lying dark singlet and its triplet counterpart.[97] Singlet–triplet degeneracies such as these have been predicted in one-dimensional excitonic models of conjugated polymers.[98] Similar to chiral nanotubes the symmetric excitons have a vanishing exchange energy which result in this degeneracy. In principle this could effect relaxation of excitons in SWNTs through efficient intersystem crossings (spin flip of an electron or hole).[99] Gaining an understanding of the role of triplet excitons in the photophysics of carbon nanotubes is still in its infancy, however recent work on polymer wrapped tubes has shown evidence of their existence.[100] In photovoltaic devices the role of these states may become important as interactions at electrodes and heterojunctions can enhance intersystem crossings.

Besides the D mode phonon-allowed E symmetry excitons, charge impurities in the form of adsorbed ions or dopants can alter the optical spectra and affect photovoltaic device performance. For example, S_1 excitons bound to dopants or localized charges on a tube can form trions $^*S_1$ which can also be created by all-optical means through exciton–exciton annihilation.[101] The trion emission can be nearly as strong or overcome emission of the S_1 exciton allowing a clear diameter and family dependence of the trion energy to be observed. Both positive and negative charged trions have been created electrochemically and were found to have identical energies because of identical effective masses of electrons and holes.[102] Moreover, recent theoretical investigations using the Bethe–Salpeter equation have shed light on the mechanisms of forming trions with ionic species in the vicinity of a nanotube and provide validity to experimentally observed diameter and family dependencies.[103] However, experimental investigations of nearly monochiral (7,5) photovoltaic devices suggests that trions have a negligible effect on performance because of the invariance of the current responsively with increasing irradiance.[104]

In theory, each E_{ii} transition can contain the fine-structures mentioned above, but effects of the ionization continuum of e–h pairs that increase in number with increasing energy may begin to mask excitonic effects.[105] As a summary we give an overview of the aforementioned excitonic states in Fig. 5a for the (6,5) tube, along with photoluminescence excitation and absorption spectra in Fig. 5b and c for a (6,5) enriched colloidal ensemble.[96,106]

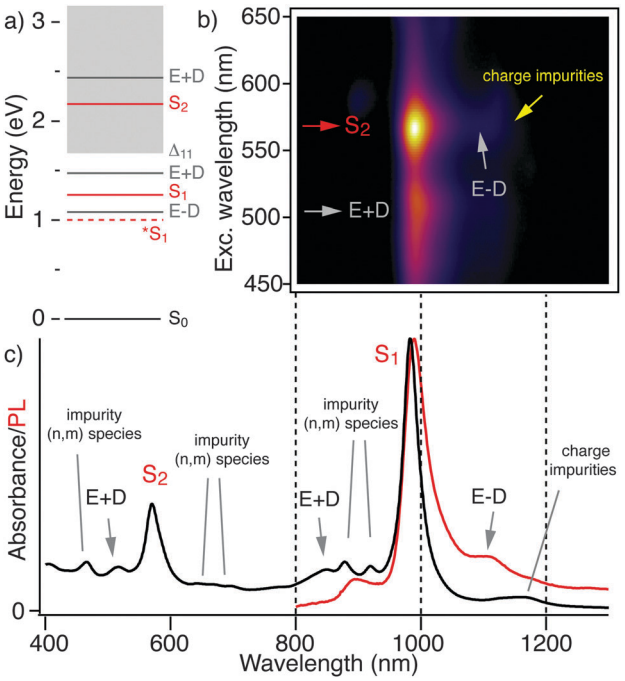

Fig. 5 (a) Schematic of the bright and grey (weakly allowed) excitonic states in a (6,5) carbon nanotube. The A_1 line symmetry excitons S_1 and S_2 are shown in red. The doubly degenerate E symmetry exciton states are shown as vibronic sidebands with a D mode phonon, and the ionization continuum of S_1 is shown as Δ_{11}. Charge impurities introduce a charged S_1 state or trion labeled $^*S_1$. (b) Photoluminescence excitation spectra of a (6,5) enriched sample showing excitation of the S_2 exciton and emission of the S_1 exciton. The vibronic sideband E + D is also shown. (c) Absorbance and fluorescence spectrum, at resonant S_2 excitation, of the same sample in (b). All of the aforementioned states are labeled with some impurity (*n*,*m*) species noted.

4 Nanotube dispersions and separations

For the most part, single-walled carbon nanotubes being used by researchers investigating bulk optical and electronic properties rely on commercial raw material sources and spend a great deal of effort in post-processing to achieve electronic purity. The three main techniques for synthesizing single-walled carbon nanotubes are arc-discharge,[107] chemical vapor deposition (CVD),[108,109] and laser ablation.[110] All of these techniques have enabled commercial sales of SWNTs, however they produce diameter distributions of tubes that contain both semiconducting and metallic species and require post-processing to achieve electronic purity. Therefore, obtaining homogeneous dispersions of SWNTs is a critical aspect of enabling mechanical, electronic, and optical applications and has motivated a significant effort in understanding and controlling SWNT surface chemistry towards generating stable SWNT solution suspensions. Strong attractive intertube van der Waals forces,[111] combined with their high aspect ratios, result in generation of tightly packed polydisperse aggregates of as-grown material. Breaking up such aggregates into individualized tubes, and their stabilization against rebundling, is essential for probing exciton photophysics *via* optical spectroscopy,[13,14] for enabling SWNT separation to isolate desired optical and electronic behaviors, and for facilitating SWNT processability to generate thin-film optoelectronic devices, each being an important aspect of enabling SWNT-based photovoltaics. Many different approaches exist for addressing this dispersion problem and include both chemically attaching dispersant molecules (covalent functionalization) and physically adsorbing molecules (non-covalent functionalization) onto the surface of the tubes. Each to some degree alters the intrinsic electronic state of the tubes and thus their observed optical and electronic properties. Therefore, selecting the dispersing method according to the desired end properties is crucial in obtaining dispersions for the anticipated application.

Because suspensions based on aggressive chemical functionalization disrupt the optical and transport properties of interest for PV needs, for the purposes of this review we highlight mild methods of dispersing SWNTs *via* non-covalent functionalization with polymers, DNA, or surfactant wrapping.[13,26,31,112,113] Although surfactants and polymers have been used extensively to disperse tubes as a route towards examining their intrinsic properties, the degree of interaction between the dispersing agents and the tubes, the surfactant structure and charge, and their concentration are known to play a crucial role in the dispersion quality. Additionally, the sensitivity of SWNT photophysical properties to environmental interactions has further motivated significant recent effort towards understanding and controlling dispersant surface structures as they relate to defining the local surface environment experienced during the dynamic evolution of the optically excited excitons.[96,114–130]

Efforts aimed at understanding dispersant surface structures and their SWNT interactions have also generated substantial results in the area of separation of tubes by chirality, length, and bundle size. Separations are an important development for enabling SWNT-based PV as they provide a tool for defining thin-film optical response, film morphology, and intertube interactions within the film. For example, chirality selection can define the optical transition energies and band offsets required for engineering desired absorption properties and directional transport of free charges at interfaces. Thus, SWNT-based thin film PV devices can now be generated from solution-phase material with desired tube compositions. Furthermore, the ability to isolate metallic *vs.* semiconducting SWNT species provides a route to eliminate metallic contamination in the light-harvesting layers that would siphon off photo-generated charge. Additionally, isolation of pure metallic species may be desirable for generating transparent collection electrodes (see Section 8). Examples of successful recent advances in separations include approaches based on ion exchange chromatography paired with selective adsorption of tailored DNA sequences,[26,33,131] density gradient ultracentrifugation (DGU),[27,28,34,106,129,132–135] gel chromatography (GC),[35,136–138] and selective suspension of specific chiralities using fluoropolymers.[31,139,140] DNA-based ion exchange chromatography is capable of exceptional enrichment of several specific semiconducting and metallic chiralities.[33,131] For active layer PV needs, separations have focused on polymer-based selective suspension due to the ability of these approaches to reproducibly produce large quantities of enriched material with no metallic impurities.[104] Whereas DGU and gel chromatography have primarily been used for generating enriched metallic species for conductive electrodes,[141] DGU is also capable of sorting nanotubes by length[142] and enables generation of defined-composition aggregates.[78] However, recent gel chromatography separations have enabled polymer free photovoltaic devices with nearly single chirality (6,5) species.[143] Therefore, GC holds promise to be a viable technique for scalable production of metal-free single chirality suspensions.

Although solution phase processing is the most cost-effective way to produce PV devices, the presence of dispersing agents such as polymers and surfactants may hinder their full potential. Vacuum filtration, spin coating, doctor-blade casting, and spray coating are the most commonly used methods of producing thin SWNT films for PV applications. Each of the techniques are being investigated for effects of film morphology on charge and energy transport processes and to some extent are specific to the character of the dispersant used in the nanotube solution. Post-processing such as thermal annealing and copious washing with water and/or organic solvents is required to remove the excess dispersing agents. Removal of polymer dispersants can be particularly challenging and the residual dispersant can limit ultimate device performance by limiting intertube charge transport towards collection interfaces and potentially by serving as exciton-trap sites.

5 Exciton dynamics

Upon the absorption of visible light a relaxation process must occur for the lower lying near-infrared exciton states of carbon nanotubes to become occupied. This conversion of energy is an

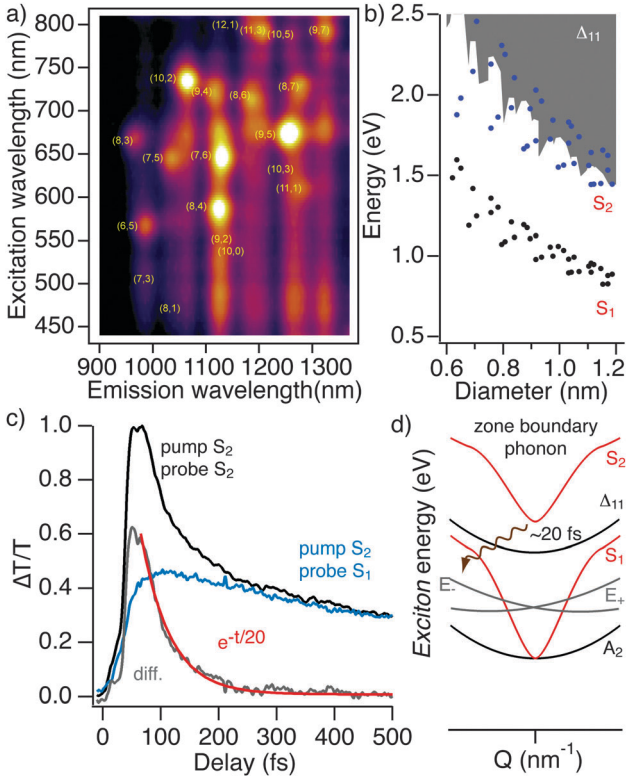

Fig. 6 (a) Photoluminescence excitation (PLE) spectra of a polydisperse sample of carbon nanotubes, different (*n*,*m*) species are labeled according to Weisman *et al.*[2] (b) Energy diagram showing the S_1 and S_2 exciton energies found from a PLE map like the one in (a), where the free particle gap Δ_{11} is determined from theoretical calculations of the exciton binding energy, adapted from Hertel *et al.*[144] Some of the S_2 excitons lie in the continuum of S_1; however the main population relaxation process of S_2 to S_1 is phonon-mediated. (c) Transient absorption kinetics for a (6,5) enriched sample pumping S_2 and probing S_1 and S_2. The delayed rise time in the scaled S_1 probe is due to a delayed population relaxation from S_2 to S_1. The difference in the two kinetics show a mono-exponential decay with a time constant of ≈20 fs indicating an S_2 to S_1 population relaxation within tens of fs, adapted from Crochet *et al.*[5] (d) Schematic of S_2 exciton population relaxation by emission of a finite momentum zone-boundary phonon that leaves the nanotube in an E symmetry exciton excited state.

essential process in PV active elements and has been investigated by both continuous wave[144] and ultrafast spectroscopies,[145] revealing a phonon mediated mechanism that is of similar character to an internal conversion in molecular systems. In the continuous wave investigation, a PLE map was generated of a polydisperse sample, see Fig. 6a, and the PLE linewidth of S_2 was examined against theoretical calculations of the position of the free particle gap Δ_{11}, see Fig. 6b. There was no correlation between these two quantities and a phonon-assisted relaxation process was modeled within the Bethe–Salpeter formalism. A one-to-one correlation with the linewidths and the calculated decay rates of an S_2 exciton emitting a finite momentum zone-boundary phonon provided a basis for assigning the internal conversion.[144] Similarly, transient absorption spectroscopy has shown that phonons must be involved in S_2 population relaxation. Other mechanisms can be excluded because of weak excitation intensity dependences of relaxation that rule out electronic mechanisms such as bi-molecular electron–electron collisions.[145] As shown in Fig. 6c, transient photobleaching measurements demonstrate that S_1 is populated within tens of fs[5] following excitation at S_2, indicating a very effective internal conversion.[144] In accordance with theory,[144] such a process leaves the system in a finite momentum E symmetry exciton state where both intra- and inter-band scattering within the E_{11} exciton manifold must take place to populate S_1, Fig. 6d.

Little is known about the exact mechanism of how S_1 becomes populated after internal conversion, but time resolved photoluminescence microscopy has pointed to a possible mechanism[96] and PV device investigations suggest that it happens with near unity efficiency.[104] Fig. 7a shows a photoluminescence image of an approximately 18 μm colloidal SWNT. The quantum yield of this tube was estimated to be a few percent using the corrected photon count rate from the imaging camera, the exposure time, and an absorption cross section per carbon atom of 1×10^{-17} cm^2 to 7×10^{-18} cm^2.[146]

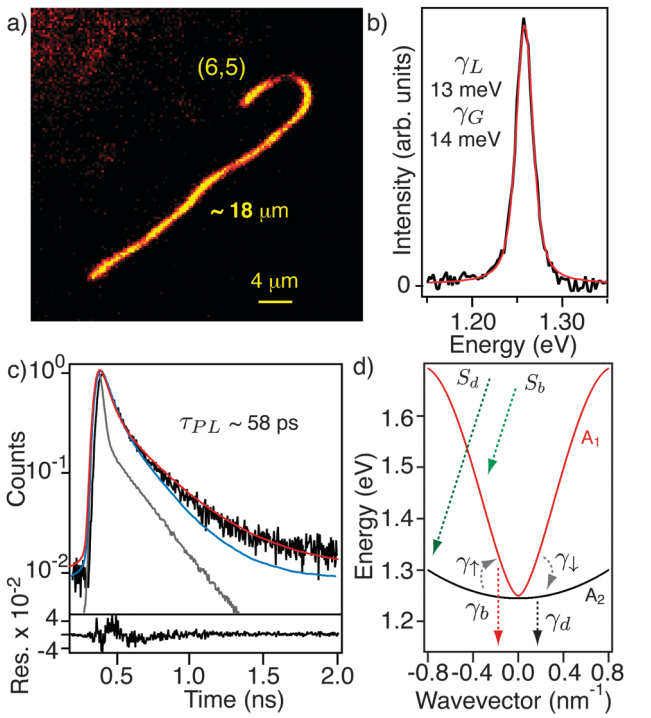

Fig. 7 (a) Photoluminescence image of S_1 emission (upon resonant S_2 excitation) of a long, colloidal (6,5) carbon nanotube, adapted from Crochet *et al.*[149] (b) Single tube photoluminescence spectrum of S_1 emission upon conical excitation resonant with S_2, adapted from Crochet *et al.*[96] (c) Photoluminescence lifetime from a single (6,5) tube (black), instrument response function (grey), and double exponential (red) and mono-exponential fits (blue). The double exponential fit is used to determine the effective fluorescence lifetime, τ_{PL}, where $\tau_1 \approx 49$ ps and $\tau_2 \approx 449$ ps. The residual of the double exponential fit is shown at the bottom of (a) and we consistently find that ≈90% of the intensity is comprised of the fast component. The mono-exponential fit has a time constant of $\tau \approx 58$ ps, adapted from Crochet *et al.*[96] (d) Exciton dispersions used in the calculation of the diffusion constant. The bright A_1 symmetry exciton is shown in red and the dark A_2 symmetry exciton is shown in black. The rates used to calculate the bright exciton distribution are also shown, where $\gamma_\downarrow$ and $\gamma_\uparrow$ are the A_1–A_2 inter-parity scattering, γ_b is the A_1 exciton decay dominated by non-radiative processes, γ_d is the A_2 exciton decay, and S_b/S_d represents A_1/A_2 exciton generation rates, adapted from Crochet *et al.*[96]

In Fig. 7b we show an emission spectrum for a single (6,5) tube with its associated Voigt fit as described by Cambré *et al.*,[147] and find that the inhomogeneously broadened Gaussian component has a width of $\gamma_G \approx 14$ meV and the homogeneously broadened Lorentzian component has a width of $\gamma_L \approx 13$ meV. The fluorescence linewidth at the single tube level is given by $\Gamma = \hbar[\tau_{PL}^{-1} + 2\tau_\phi^{-1}]$, where τ_{PL} is the effective lifetime for population decay and τ_ϕ is the pure dephasing time describing the mean free time between decohering scattering events. The inhomogeneous broadening arises from spectral wandering as the colloidal interface is dynamic and provides an inhomogeneous dielectric environment.[96] In Fig. 7c we show a fluorescence lifetime for a single (6,5) tube with its associated fit. The time dependence of the fluorescence intensity is systematically bi-exponential for these types of samples and fit by $I(t) = (Ae^{-t/\tau_1} + Be^{-t/\tau_2})$, where τ_1 and τ_2 are time constants weighted by A and B, convoluted with the instrument response function (IRF) of the time-correlated single photon counting system.[146,148] As reported previously,[146,148] the long component τ_2 with a weight of $B\tau_2/(A\tau_1 + B\tau_2)$ accounts for $\approx$10% of the total fluorescence intensity. The effective fluorescence lifetime was then calculated as a weighted average $\tau_{PL} = \int I(t)dt = (A\tau_1 + B\tau_2)/(A + B)$, and represents the effective bright exciton lifetime of $\approx$58 ps.[96]

It is known that the A_2 and A_1 symmetry excitons can interparity scatter due to A line group symmetry breaking with rates given by $\gamma_\uparrow$ and $\gamma_\downarrow$, however, this process is known to be slow when compared to the lifetimes of both parity excitons.[146,148] Here $\gamma_\uparrow = \gamma_0 n(\Delta)$ and $\gamma_\downarrow = \gamma_0[n(\Delta) + 1]$, where n is the Bose–Einstein distribution function and γ_0 is the zero temperature scattering rate. For small γ_0 compared to other decay processes this behavior results in a non-equilibrium distribution between the states largely responsible for the bi-exponential behavior shown in Fig. 7c,[147,148] and has also been shown directly by low-temperature photoluminescence spectroscopy at the single tube[94] and ensemble levels.[95] To account for the distribution between A_1 and A_2 excitons as well as other processes including the generation of S_b and effective decay γ_b of A_1 excitons and the generation of S_d and effective decay γ_d of A_2 excitons, the population of the bright state at $q = 0$ is calculated by the steady state solution to the system in Fig. 7d. In order to fit the dynamics, the exciton generation rates must take the form $S_b = S_d$,[148] which suggests that upon relaxation from S_2 there is a rapid scattering mechanism that populates the E_{11} manifold. However, scattering between the states must be very limited for the S_1 lifetime to be bi-exponential. Using parameters that describe the bi-exponential decay of the photoluminescence: $\gamma_d = 2$ ns^{-1}, $\gamma_b = 20$ ns^{-1}, and $\gamma_0 = 0.05$ ns^{-1},[148] we find that at steady state the probability of finding an exciton in the bright state $\eta_b \approx 11\%$ is much smaller than the probability of finding an exciton within the dark state $\eta_d \approx 89\%$. This places an upper limit on the fluorescence quantum yield and may partially explain why emission efficiencies are so low in these systems.[106]

Exciton diffusion is known to be important for nanotube photophysics[45,96] and leads to population loss of S_1 through interaction with quenching sites along the tube backbone and at tube ends *via* non-radiative decay. Moreover, energy transport is important for photovoltaics where heterojunctions provide an interface for exciton dissociation.[21] Diffusion lengths can be extracted directly from exciton quenching by the nanotube ends, Fig. 8a, and have typical median values of $l_D \approx 200$ nm in colloidal tubes.[96] This result is nearly the same as the diffusion length of excitons in larger diameter tubes in laboratory air,[150] which suggests that excitons may experience similar transport mechanisms in atmospheric environments where several monolayers of adsorbates are present. With a median fluorescence lifetime of $\tau_{PL} \approx 55$ ps an exciton diffusion constant, $D = l_D^2/\tau_{PL}$, was determined to be $D \approx 7.5$ cm^2 s^{-1}.[96] By including only rapid intra-band thermalization of S_1, because of the weak inter-parity scattering, it was found that interface scattering or a disordered environment dictates the exciton diffusion constant. In this regime, an exciton wave-packet moves with a certain transport velocity v and is scattered by an inhomogeneous surface potential provided by the dynamic colloidal interface. Such motion is derived from standard theory of waves propagating in strongly scattering media and is described by a mean free path ξ such that $D = v\xi$.[151] Here, the transport velocity is given by the thermally averaged group velocity $v = \langle|v_{b,q}|\rangle$ calculated from the exciton dispersion in Fig. 7d and at room temperature we find $v \approx 0.5$ nm fs^{-1}. In order for $D \approx 7.5$ cm^2 s^{-1} the mean free path must be $\xi \approx 1.5$ nm. As a theoretical comparison, the predicted exciton correlation length, full width-half maximum

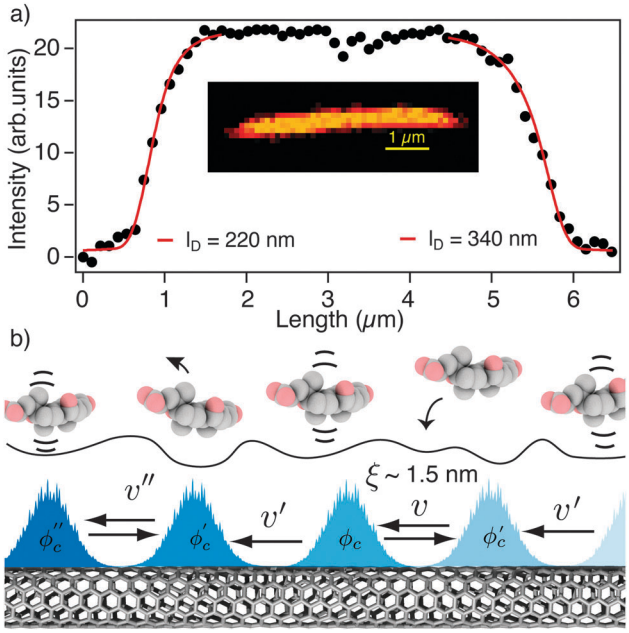

Fig. 8 (a) Intensity cross-section parallel to a tube axis (black circles) from the image in the inset where the fit (red) is the solution of the 1D diffusion equation convoluted with the Airy disk that described the point spread function of the microscope.[96] (b) Schematic of exciton transport for disorder limited case. An exciton wave-packet, described by a Gaussian electron–hole pair probability distribution of width σ, moves with a velocity v and scatters at a lattice site through the disorder potential in (a) where the exciton velocity changes to v'. Within the coherence length ξ the phase of the wavefunction ϕ_c is preserved, adapted from Crochet *et al.*[96]

of the nearly Gaussian envelope function, of a (6,5) nanotube embedded in an effective dielectric constant of κ = 1.85 is $\sigma \approx 1.5$ nm.[97] This suggests that the exciton travels, on average, a distance equal to the width of a distribution function describing the probability of finding an electron or a hole at a fixed hole or electron position. Moreover, excitons are coupled to the local environment such that a scattering event can take place on average at every distance ξ which gives an upper estimate for the linear packing density of the colloidal interface or the molecules adsorbed onto the surface.

Even though intratube exciton transport as outlined above is not intrinsic to exciton–phonon scattering, this shows that even in a disordered environment S_1 excitons can travel 100s of nm at room temperature to reach an interface where dissociation may take place for photovoltaic applications. As pointed out above the dark exciton seems to be populated for a longer time and it can also be transported to an interface, however its mobility is reduced as compared to the bright exciton. Since the thermally averaged group velocity of an exciton with a parabolic dispersion, free particle with kinetic energy k_BT, is given by $v = \sqrt{2k_BT/m^*}$, we can expect that for a dark exciton with an effective mass of m^* = .435m_e and mean free path ξ = 1.5 nm, $D \approx 2.2$ cm^2 s^{-1} at room temperature. This implies that $l_D = \sqrt{D\gamma_d^{-1}} \approx 330$ nm, which is over 100 nm longer than l_D for the bright exciton. Therefore, the bright and dark excitons have diffusion lengths that are 100s of nm and energy transport along the tube backbone may be unaffected by such a large steady state population of excitons in the dark state. The transport of other excitonic states such as triplets or trions is yet to be explored, but it can be expected that the lifetimes of triplets should be much longer and may have diffusion lengths much longer than their singlet counterparts.

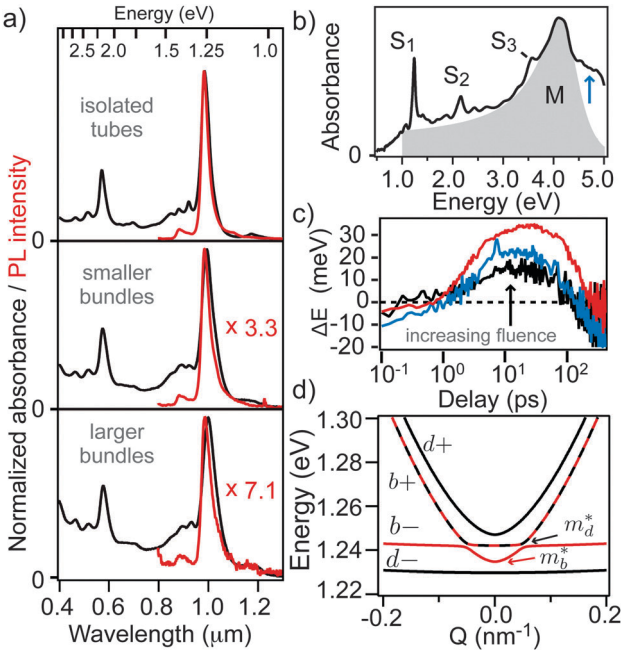

Fig. 9 (a) Normalized absorption and photoluminescence spectra of selected fractions from a selectively aggregated (6,5) enriched sample sorted by bundle size, adapted from Crochet *et al.*[78] An increase in the non-resonant absorption strength underneath of S_2 is apparent as well as a blue-shifted fluorescence from S_1 relative to S_1 absorption. (b) Absorption spectrum of a composite film of (6,5) enriched nanotubes in gelatin. The exciton resonances S_i are labeled and the grey shaded region is a Fano fit to the M point exciton arising from the interference of a discrete state and the e–h pair continuum, adapted from Crochet *et al.*[5] (c) Dynamic blue-shift of S_2 due to the presence of delocalized e–h pairs created upon UV excitation, adapted from Crochet *et al.*[5] (d) Dispersions for an excitonically coupled carbon nanotube dimer. The state labeled b− is strongly dipole allowed while b+ is weakly allowed. The weakly allowed bright state dominates the emission spectrum because of its long lifetime, adapted from Crochet *et al.*[78]

6 Excitons and free carriers in bundled nanotubes

The incorporation of carbon nanotubes into thin film devices has relied on self-assembled layers that have been purified in a certain electronic type[152] or diameter distribution.[133] Polymer free active layers also rely on the physics of intertube interactions.[143] As mentioned above, self-assembled tubes are strongly bound in aggregates that display altered electrical and optical properties. For example, within a nanotube bundle an increase of the dielectric function ε relative to an isolated tube can result in a mutual screening of the intra-tube Coulomb interactions. In particular, a reduction in the strength of the electron–hole interaction can renormalize the exciton oscillator strength. This effect is well known in one-dimensional semiconductors where increasing the spatial cutoff of the effective one dimensional Coulomb interaction, which accounts for screening, can result in a loss of exciton oscillator strength to band-to-band transitions.[153]

Recent work on selective aggregation and bundle size sorting of (6,5) tubes, see Fig. 9a, found an increased response of the free carrier continuum relative to isolated tubes.[78] Fig. 9b shows the ground state absorption spectrum of bundles containing a majority of (6,5) tubes in a SWNT-gelatin film. The exciton resonances S_1–S_3 can be observed at 1.25, 2.16,[14] and 3.6 eV (ref. 154) residing on a broad background culminating at the $\pi \rightarrow \pi^*$ transition at approximately 4.3 eV. Motivated by recent investigations of the M point exciton in graphene,[155] we fit this feature with a Fano profile $A(E) \propto (q + \varepsilon)^2/(1 + \varepsilon^2)$ where $\varepsilon = (E - E_r)/(\Gamma/2)$. Here q^2 defines the ratio of the strength of the excitonic transition to the free $\pi \rightarrow \pi^*$ transition, E_r is the exciton resonance energy, and Γ corresponds to the exciton lifetime.[155] It was found within this model that E_r = 4.28 eV, Γ = 860 meV ($\approx$5 fs), and $q = -2.83$ fits the shape of the underlying absorbance sufficiently up to approximately 1 eV.

Using transient absorption spectroscopy, it was also found that the spectral position of the S_2 (for UV excitation, as opposed to low energy excitation) was strongly time dependent. As shown in Fig. 9c, the spectral position was dynamically shifted with respect to the S_2 ground state absorption energy and depended strongly on fluence. The S_2 energy was initially red-shifted by 10s of meV and within 20 ps was blue-shifted to a maximum of 10s of meV followed by a slow recovery back to the ground state energy. Electric field effects in 1D excitonic

systems have been predicted to include strong field strength dependent broadening and spectral shifts.[156] Within the quadratic Stark effect description, the shift (ΔE_x) of the ground state exciton energy (E_x) can be expressed as $\Delta E_x = \sum_j |\vec{\mu}_j \cdot \vec{F}|^2/(E_x - E_j)$ where $\vec{F}$ is the electric field strength and $\vec{\mu}_j$ and E_j are the dipole moment and energy of continuum state j. The denominator of ΔE_x determines the sign of the shift, where coupling to higher or lower energy continuum states results in a red- or blue-shift, respectively. Here, ionization of M point excitons initially lead to a finite population of high energy continuum states that red-shift S_2. At later times, a sign change in ΔE_x indicates that lower energy continuum states within the energetic range S_2 are populated after interband relaxation. The strong fluence dependence of the shift of S_2 is understood from the strong field dependence of ΔE_x, in which F is proportional to the local charge density excited by the pump pulse and stabilized within an aggregate. The magnitude of F can be estimated from the Stark shift of one-dimensional Wannier excitons, $\Delta E_x \approx 9e^2r_0^2F^2/8E_b$,[157] where $E_b = 350$ meV is the exciton binding energy and $r_0 = 1.0$ nm is the exciton radius, Fig. 9c. From the maximum blue-shift of S_2 we estimated field strengths of up to $F \approx 100$ V μm^{-1}, which is consistent with previously measured SWNT Stark shifts by the displacement photocurrent technique.[158] Interestingly, if this effect can be incorporated into thin film photovoltaics, the need for an interface for excitons to dissociate may be negated as both light absorption and charge generation can take place in the same material layer.

Besides an increased response of the free e–h pair continuum, evidence of coherent intertube excitons has been presented.[78] The blue-shift of the fluorescence with respect to S_1 absorption shown in Fig. 9a is commonly observed in H-type molecular aggregate systems that can be described by point dipoles.[159] However, in the case of carbon nanotubes the physical picture is more complex because of the underlying symmetry of the graphene lattice and the presence of delocalized transition densities.[78,160,161] Interestingly the exciton lifetime measured by time-resolved fluorescence was also found to increase for this blue-shifted emission,[78] suggesting that a new exciton state was being formed upon aggregation. To describe such a state, a model Hamiltonian was derived including the effects of intertube exciton tunneling of bright A_1 and dark A_2 excitons. A two peaked absorption spectrum can be expected, with upper and lower bright delocalized excitons having relative energies and oscillator strengths of $E_{b+} = -8$ meV, $f_+ = 0.2$ and $E_{b-} = -15$ meV, $f_- = 1.8$, respectively, see Fig. 9d. Two dark excitons were also found, having energies of $E_{d+} = -3$ meV and $E_{d-} = -20$ meV. Beyond the observed effects on the absorption and fluorescence spectra, this observation is important for photovoltaics made of nanotube bundles. Specifically designed nanotube aggregates or artificial molecules can be designed with selective aggregation and density gradient ultracentrifugation as preparative tools. As a result, investigating exciton delocalization in engineered carbon nanotube aggregates may provide model systems for coherent energy transport in natural light harvesting systems,[162] and prove to be an efficient means to transport energy parallel to the tube axis.

7 Nanotube photocurrent as a probe of exciton dissociation

As noted above, optical absorption in SWNTs occurs primarily through the creation of bound excitons, rather than through the creation of free electron–hole pairs.[37,73,163] High exciton binding energies raise important issues on the use of carbon nanotubes as photoactive (light absorber) elements for optoelectronic applications like photovoltaics and photodetectors. Since optical excitations in SWNTs create strongly bound electron–hole pairs, this should block the generation of free carriers and limit the sensitivity of the SWNT photocurrent response. Thus, understanding exciton dissociation processes both in individual SWNTs and in their films is critical before they can be incorporated into the above-mentioned optoelectronic devices. In spite of strong Coulombic interactions, it has been demonstrated that efficient exciton dissociation in individual SWNTs can be encouraged by applying an electric field (internal fields such as in p–n junctions[164] and Schottky barriers[165,166]). Reasonable effort has gone towards understanding the influence of electric fields on the nanotube optical response. In three-dimensional semiconductors, electric fields cause a Stark shift in the absorption maximum and a modulation in the absorption coefficient.[167] Perebeinos *et al.* predicted a strong modulation of the absorption spectrum with increasing electric field in individual SWNTs.[156] The exciton formation rate due to impact ionization is also exponentially dependent on the electric field, and increases dramatically for potentials above the optical phonon energy.[164,168] Importantly, the electric field also provides a mechanism by which the excitonic states can be dissociated into free carriers (similar to the field induced ionization observed in atomic systems[169]). Field-induced exciton dissociation should have a measurable effect on the nanotube photocurrent. At zero electric field, bound charge carriers cannot contribute to the photocurrent unless they relax to a lower energy free carrier state. Electric fields provide a dissociation mechanism that effectively ''turns-on'' the ground state excitonic transition in the photocurrent spectrum. This is in contrast to exciton dissociation of higher energy transitions where optically generated excitons are thought to decay to lower energy continuum states that then contribute to the observed photocurrent. In this way, free and bound charge transitions in the optical spectrum can be distinguished, and the influence of electric fields on either type of transition can be explored. All of these processes are important for photovoltaics where interfaces of materials can lead to strong internal fields that facilitate the generation of free electron–hole pairs from excitons.

In this section we describe the results of an innovative direct probing photocurrent technique known as the Capacitive Photocurrent Spectroscopy (CPS)[158,170–173] that allows measurement of the excitation spectrum of individual nanotubes while applying large electric fields. Fig. 10a shows the measurement setup. Individual single walled nanotubes (SWNTs) were grown by chemical vapor deposition on an oxidized p^{++} silicon substrate, Fig. 10b. A 25 nm thick layer of ITO is

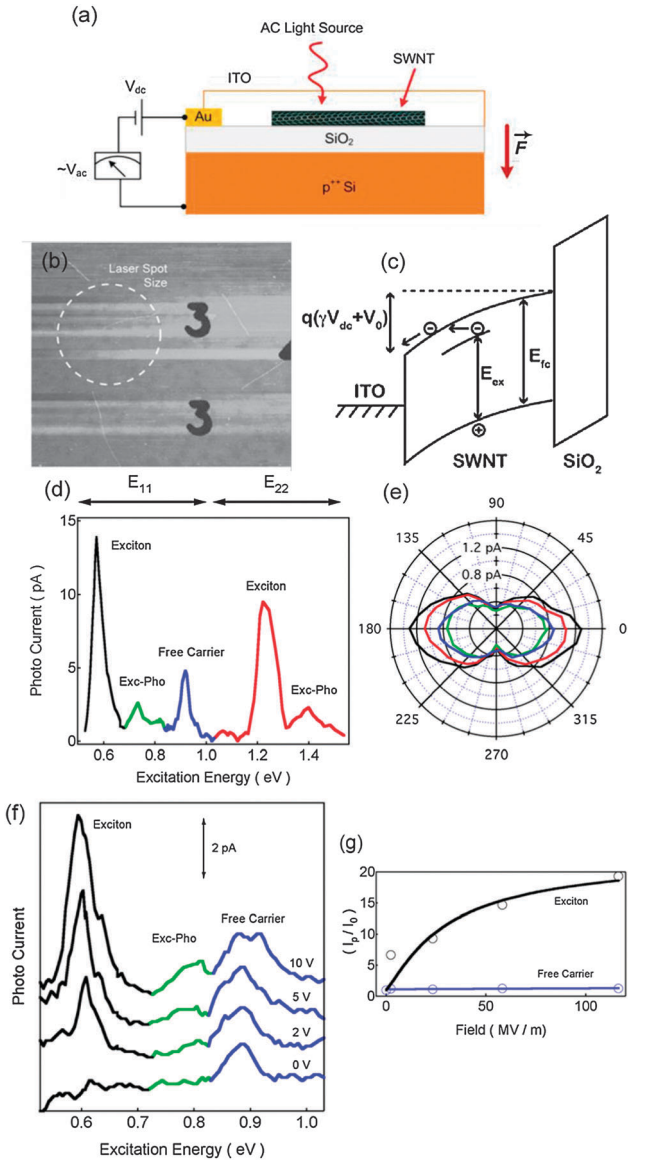

Fig. 10 (a) Schematic of device used to measure capacitive photocurrent of individual carbon nanotubes. (b) Atomic force microscope image of the top surface of the device showing the nanotube density and laser spot size. (c) Simplified band diagram of the ITO/SWNT/oxide structure showing the lowest order free carrier E_{fc} and excitonic E_{ex} transitions. (d) Photocurrent *versus* excitation energy for an individual nanotube measured with 20 V dc bias across the capacitor. (e) Polarization angle dependence for the four largest photocurrent peaks. (f) Photo current *versus* excitation energy measured near the S_1 exciton transition for bias ranging from 0 to 10 V. The curves are offset for clarity. The apparent splitting in the free carrier peak at 10 V is not reproduced in other devices. (g) Normalized photocurrent *versus* electric field of the excitonic and free carrier peaks. Figure adapted from Mohite *et al.*[158]

deposited by electron beam evaporation, creating a transparent Schottky contact to the nanotubes. As shown in Fig. 10a, the final device structure is a capacitor with a heavily doped silicon back electrode, a silicon dioxide dielectric, and an ITO top electrode. Applying a dc bias across the capacitor creates an electric field perpendicular to the nanotube axis. To probe the nanotube photoexcitation spectrum, pulsed laser light was directed at a single carbon nanotube lying at the ITO/oxide interface.

The mechanism for photoexcitation and charge carrier detection can be understood by considering the simplified band diagram shown in Fig. 10c. The lowest order free carrier and excitonic transitions in the nanotube are denoted by E_{fc} and E_{ex} respectively. V_o is the built-in potential which exists at the SWNT/ITO interface, and which arises from the unequal chemical potential between the SWNT and ITO. If light is absorbed by a carbon nanotube to create electron hole pairs, the charge will tend to separate due to this built-in Schottky barrier potential. For a p-type nanotube, holes will drift into the ITO, while electrons will drift toward the oxide interface. The charge separation produces an ac displacement current across the ITO/Si capacitor, which can be measured with a lock-in amplifier, synched to the laser repetition rate. The displacement photocurrent signal requires optical excitation of charge carriers followed by physical separation of the excited charge.[158] The technique is thus sensitive to optical excitations in which freely mobile charge carriers are created. Another advantage is that it is straightforward to characterize individual nanotubes by increasing the spacing between nanotubes on the sample surface so that it is larger than the laser spot size.

Application of an electric field increases the band-bending across the carbon nanotubes. Similar effects can be expected at an interface of nanotubes and other materials, thereby increasing the carrier capture efficiency. Because of the capacitor structure, it is possible to apply large electric fields without generating appreciable dark current. The electric field across the nanotube for an applied bias V_{dc} was estimated by considering the nanotube as an insulator with a dielectric constant κ_{nt} = 3.38 and thickness T_{nt} = 1.3 nm lying on the silicon dioxide insulator with dielectric constant κ_{ox} = 3.9 and thickness T_{ox} = 100 nm. The electric field across the nanotube is then given by:

$$F_{nt} = \frac{V_{dc}\kappa_{ox}}{T_{nt}\kappa_{ox} + T_{ox}\kappa_{nt}}. \quad (3)$$

For a maximum applied bias of 32 V this gives $F_{nt} = 3.7 \times 10^8$ V m^{-1}, and a band offset across the width of the nanotube of V_{dc} = 0.48 eV. This is large enough to appreciably influence charge transport across the nanotube/ITO interface. Fig. 10d shows the photocurrent measured for a typical nanotube at the ITO/oxide interface with an applied bias of V_{dc} = 20 V. A number of peaks are observed as a function of laser excitation energy. Evidence that we are measuring an individual nanotube is provided by the polarization dependence of the photocurrent, shown in Fig. 10e. Each of the four main peaks observed in the photocurrent show strong polarization dependence, and are maximized at the same polarization angle as expected for a one-dimensional electronic system.[53,76]

Fig. 10f shows the photocurrent measured in the regime of the S_1 exciton for a range of applied biases. At 0 V bias only a single peak is observed near 0.88 eV on top of a broad background. This suggests that a photocurrent is generated by dissociating excitons with a built-in field across the interface.

At higher bias, a second peak emerges near 0.61 eV. The magnitude of the lower energy peak increases with increasing bias and eventually overshadows the higher energy peak. Fig. 10g shows the normalized photocurrent measured for both the lower and higher energy peaks. The higher energy peak changes little with the applied field while the lower energy peak shows a large increase. In addition, the lower energy peak is accompanied by a phonon satellite peak, which is approximately 185 meV higher in energy than the main peak position. (This is similar to the exciton–phonon satellite peak observed around S_2.) This suggests that the lower energy peak is the S_1 excitonic state, while the higher energy peak is the ground state free carrier transition. (This assignment also agrees with absorption measurements made on carbon nanotube films.[172]) A similar peak structure was observed in four different semiconducting nanotubes. One can extract the S_1 exciton binding energy by taking the energy difference between the excitonic and band-to-band photocurrent peaks. For the spectra in Fig. 6 this gives 0.274 eV, while binding energies ranged from 0.270 eV to 0.300 eV for the four nanotubes measured. These values agree with theoretical predictions, assuming a nanotube diameter of 1.3 nm and a dielectric constant $\kappa_{nt} = 3.38$.[174]

The field dependence of the S_1 transition can be understood using a field enhanced tunneling model,[172,175] which assumes a constant field across the width of the nanotube. As shown in Fig. 10f, the electric field brings the energies of the free carrier and bound carrier states into alignment. Bound carriers can then dissociate into free carriers by tunneling into the continuum through the barrier created by the exciton binding energy. Increasing the electric field acts to reduce the tunnel barrier width, and consequently increases the tunneling rate. In this case, the photocurrent is given by:

$$I_p = I_0 \exp\left[\frac{a}{1 + b/V_{dc}}\right] \quad (4)$$

where I_0 is the photocurrent at zero applied voltage and a and b are fitting parameters related to intrinsic properties of the nanotube and the nanotube/ITO interface.[172] The solid line in Fig. 10g is a fit of eqn (4) to the experimental data points. It is seen that the tunneling model provides a good description of the S_1 exciton field dependence in the bias range of 0 to 10 V.

In addition to measuring exciton binding energies in SWNTs, CPS has been applied to the measurement of exciton binding energies in double-walled nanotubes,[170] graphene oxide,[176] organic interfaces[177] and InN nanowires.[178] In each case, details were obtained on the charge dissociation processes that were not available from conventional optical techniques. Specifically in organic solar cells the exciplex (or charge transfer state) was observed that is formed when an exciton is formed such that an electron and hole are delocalized on different materials. This information was critical in understanding the complex nature of multi-step charge transport pathways critical for the design of efficient organic devices and makes it possible to understand such photo-physical processes in SWNT-based photovoltaic devices.

8 Transparent conducting SWNT electrodes for photovoltaics

The potential of carbon nanotube thin films to serve as transparent conducting electrodes was first demonstrated by Wu *et al.*[179] This seminal work sparked a great deal of research in the following years that continues to this day. This section covers a series of studies devoted to understanding both the fundamental optical and electrical properties of single-walled carbon nanotube transparent conductors (SWNT TCs), as well as the factors that affect the performance of SWNT TCs in PV devices.

Early attempts were made to incorporate SWNT TCs into PV devices, starting in 2006 with organic photovoltaic (OPV) devices. These proof-of-concept studies demonstrated OPV devices with AM 1.5 power conversion efficiency (PCE) of $\approx$1.5%.[180] Shortly thereafter, these SWNT TCs were incorporated into inorganic PV devices, demonstrating modest success.[181,182] $CuIn_{1-x}Ga_xSe_2$ (CIGS) solar cells, in which a SWNT TC was used to replace the ZnO TC, demonstrated a maximum PCE of 13%.[182] CdTe solar cells, in which a SWNT TC was used as a semi-transparent back contact, demonstrated a maximum PCE of 12.4%.[181] These early studies demonstrated the proof of concept for using SWNT TCs in a variety of different PV technologies, but in each case, the SWNTs performed below the levels achieved using traditional TCOs. A significant amount of research in the following years sought to understand and manipulate the numerous factors that determine the fundamental optical and electrical properties of SWNT TCs.

The two most important roles played by a transparent conductor in a solar cell are to transmit as many photons to the active layer as possible and to efficiently collect one type of charge carrier (electron or hole). SWNT TCs are best understood as an intertwined network of individual SWNTs. As such, light transmission and charge transport must be considered both within the context of individual SWNT properties and collective properties of SWNTs within the film. The absorption and transmission of light are controlled primarily through the excitonic optical resonances of either semiconducting or metallic SWNTs. The conductivity σ of the SWNT TC is determined by the density η_i and mobility μ_i of charge carriers through $\sigma = \eta_i\mu_i$, where the subscript i denotes the particular charge carrier in question, either electrons (i = e) or holes (i = h). The mobility is determined by the effective mass m_i^* and average scattering time $\bar{\tau}$ by $\mu_i = e\bar{\tau}/m_i^*$. The most important parameter contributing to the carrier density is the SWNT joint density of states, Fig. 10a. Metallic SWNTs have a finite density of states at all energies, and have appreciable free carriers at the Fermi level even in an intrinsic state. In contrast, semiconducting SWNTs have a true band gap, with no states in between the first electron and hole van Hove singularities. As such, an intrinsic s-SWNT has no free carriers at the Fermi level, and should be electronically insulating and as stated above have strong excitonic effects.

Importantly, however, s-SWNT conductivity can be turned on by adsorption of molecular charge transfer dopants, which

lower or raise the Fermi level into a van Hove singularity, introducing appreciable free carriers for conduction, Fig. 11a. The adsorption of acidic molecules (*e.g.* HNO_3, $SOCl_2$ amongst many others) leads to a net withdrawal of electrons from the SWNT π network and lowers the Fermi level deep into the hole van Hove singularities, creating a p-type s-SWNT.[183] Basic molecules, such as a wide variety of amines (*e.g.* hydrazine, ethylenediamine, *etc.*) donate electron density to the pi network, creating an n-type SWNT.[184] Importantly, molecular charge transfer doping is achieved solely by physisorption of acidic or basic molecules to the SWNT surface. No covalent bonds are formed, leaving sp^2 hybridization, and the associated delocalized pi electron network, intact. Charge transfer doping plays the important role of degenerately doping the s-SWNTs, such that they display metallic-like conductivity that can be tuned to be of either n-type or p-type. Furthermore, the degenerately doped s-SWNTs actually have a higher density of free carriers at the Fermi level, and are thus more conductive, than either doped or intrinsic m-SWNTs.[183] Another important role of the molecular charge transfer dopants is to reduce the optical density of the excitonic transitions of s-SWNTs due to the state-filling effect, Fig. 11b. This effect dramatically increases the transparency of SWNT films in the visible and near-IR regions, making them more suitable for use as TCs.

Although the mobility of carriers in isolated SWNTs is extremely high, junctions between SWNTs limit the carrier mobility in SWNT TCs.[3,183,185,186] Temperature-dependent resistance measurements demonstrate activated transport, with sheet resistance decreasing with increasing temperature for films comprised of both s-SWNTs and m-SWNTs,[185] Fig. 11c. At first glance, such behavior would not be expected for an m-SWNT film, since phonon backscattering in metallic systems causes resistance to increase with increasing temperature. Considering the importance of each nanotube–nanotube junction as a barrier to charge transport, or alternatively as a resistor in an equivalent circuit, resolves this seeming inconsistency. Regardless of the SWNT type, conductivity is primarily controlled by thermally assisted tunneling through barriers at the inter-tube or inter-bundle junctions.[185] Importantly, molecular charge transfer doping was shown to decrease the magnitude of inter-tube barriers.[183,185] The magnitude of inter-tube barriers was found to be largest for films comprised primarily of undoped s-SWNTs, followed by undoped and doped m-SWNTs, and the lowest barriers were found for doped s-SWNTs.[185]

A terahertz spectroscopy study complimented these temperature-dependent measurements, demonstrating a frequency-dependent conductivity best described by a Drude–Smith model for both m-SWNT and s-SWNT films.[186] The Drude–Smith model treats the conductivity as a sum of the contributions of both localized (*i.e.* confined to individual SWNTs) and quasi-free (delocalized over several SWNTs) carriers. The Drude–Smith analysis yielded average scattering times $\bar{\tau}$ in the range of 52 to 68 fs for intentionally or adventitiously doped s- and m-SWNT TCs, indicating a mean free path of ~50 nm, which was roughly the average distance between tube–tube junctions.[186] Taken together, the temperature-dependent and terahertz measurements indicate that the conductivity of SWNT TCs is best understood by considering the dominant contribution of inter-tube or inter-bundle junction resistance. Reducing the magnitude of the transport barriers experienced by carriers at these junctions, *e.g.* by charge transfer doping or other modifications, is a critical strategy for optimizing the conductivity of SWNT TCs. A complimentary strategy involves reducing the number of junctions experienced by carriers by using SWNTs that are kept as long as possible through minimal processing.[3]

Temperature-dependent resistance measurements also revealed an important drawback of strategies employing charge transfer doping to increase SWNT TC conductivity.[185] After heating SWNT TCs to ~450 K, significant hysteresis was observed for the sheet resistance on the cool-down back to 100 K, indicating an irreversible loss of conductivity. This hysteresis was traced to the thermal desorption of either

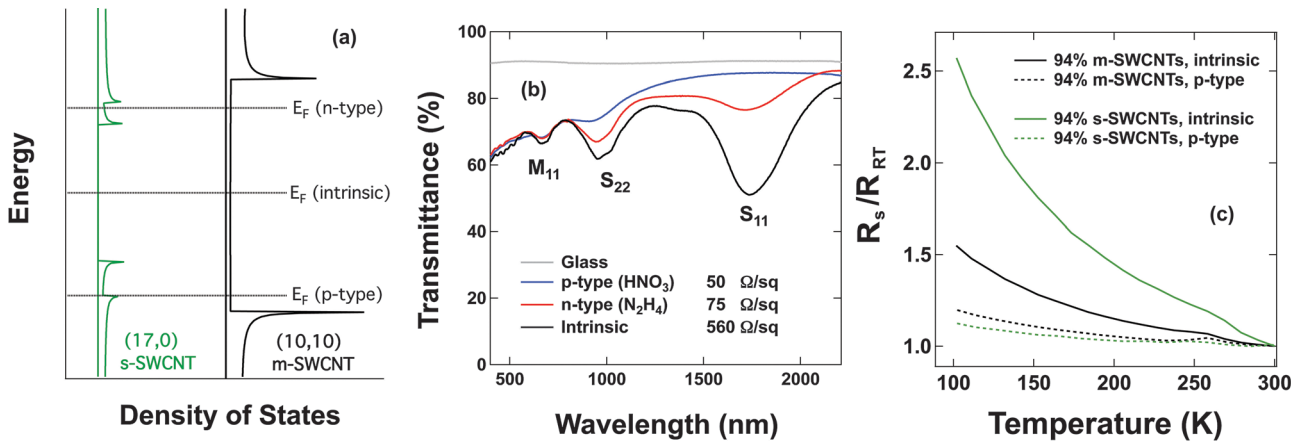

Fig. 11 (a) Calculated density of states (DOS) for representative 1.35 nm diameter SWNTs. DOS are displayed to scale. Dashed lines show approximate positions for SWNT Fermi levels (EF) when doped n- or p-type by molecular charge transfer dopants. (b) Transmittance spectra for an unseparated (2 : 1 semi : metal) SWNT thin film doped n-type by hydrazine, doped p-type by nitric acid, or in an intrinsic state (treated with N_2H_4 followed by air exposure). All spectra are recorded without subtraction of the glass substrate (shown in gray). Sheet resistance values are given in the legend. (c) Temperature-dependent sheet resistance measurements for SWNT thin films enriched in s- or m-SWNTs and either doped p-type by thionyl chloride or in an intrinsic state.

adventitious (*e.g.* ambient water, oxygen, *etc.*) or intentional (*e.g.* $SOCl_2$ or HNO_3) charge transfer dopants. Films that were heated to 450 K for enough time to fully desorb physisorbed dopants showed no hysteresis upon further cycling and recovered the full optical density of s-SWNT optical transitions. Thus, the utilization of doped SWNT TCs requires careful consideration of the instability of thermally labile dopants and/or the search for new thermally stable dopants.[185] Importantly, some molecules are more stable than others; $SOCl_2$ was found to be more stable than HNO_3,[185] and more recently, triethyloxonium hexachloroantimonate was found to be a particularly stable alternative.[187]

For the ultimate adoption of SWNT TCs into thin-film PV applications, it is imperative to develop scalable deposition methods that can be incorporated into roll-to-roll fabrication lines. Such deposition methods include spray deposition, ink-jet printing, gravure printing, and slot die coating. We developed an ultrasonic spray deposition method based on aqueous SWNTs dispersed by carboxymethylcellulose (CMC).[3] CMC disperses large amounts of SWNTs even after very short sonication times (*e.g.* 10 minutes), affording average SWNT lengths well over 1 μm. Since percolation in SWNT films is influenced by length, the SWNT TC conductivity increased significantly as a function of SWNT length, and SWNT inks sonicated for only 10 minutes produced TCs with extremely low percolation thresholds, 0.01 μg cm^{-2}.[3] SWNT TCs produced by ultrasonic spraying also demonstrated significantly lower surface roughness (3 nm rms roughness) than films produced by vacuum filtration.[179] Vacuum filtered films contained large features on the order of 100–150 nm, which are on the same scale as the active layer thickness of typical OPV active layers. Accordingly, nearly all of our attempts to produce OPV devices on vacuum filtered SWNT TCs resulted in short-circuited devices. In contrast, SWNT TCs produced by ultrasonic spraying enabled highly reproducible OPV device fabrication. The OPV device stack consisted of a SWNT TC, a PEDOT:PSS hole transport layer (HTL), the P3HT:PCBM active layer, and an aluminum back contact. OPV devices prepared on SWNT TCs demonstrated a PCE of around 3.1%, while devices prepared on ITO around 3.6%. The achieved value of 3.1% was significantly higher than previously reported PCE values for OPV devices incorporating SWNT TCs,[180,188] and demonstrated the potential for ultrasonic spraying of SWNT TCs for high quality opto-electronic devices.[3]

A subsequent study employed a more rigorous comparison of the device physics for OPV cells incorporating SWNT TCs or ITO, illuminating several important differences.[189] We found that the PEDOT:PSS HTL increased the work function Φ of ITO and decreased the device series resistance R_{ser}. In contrast, PEDOT:PSS lowered R_{ser} and increased R_{ser} for SWNT TCs. Accordingly, SWNT TCs enabled relatively efficient devices without the PEDOT:PSS HTL (2.65–3.37% PCE), whereas ITO devices without the HTL performed very poorly (1.44% PCE). However, SWNT TCs produced devices with consistently lower shunt resistance R_{sh} than ITO devices, likely caused by intercalation of the active layer into the porous SWNT TC. PEDOT:PSS coating increased R_{sh} by an order of magnitude for SWNT TCs, suggesting that the HTL may planarize the electrode and eliminate parasitic parallel current pathways.

As with any PV technology, it is important to maximize efficiency and minimize cost, in order to minimize the cost of delivered power ($/W). SWNT TCs require further improvements in performance and demonstrations of low-cost mass production for their eventual incorporation into PV devices. SWNT TCs are one alternative in a growing portfolio of nanostructured transparent conducting electrodes that includes graphene thin films and metallic nanowire networks.[190] It is likely that each of these technologies will find their way into different application niches in the near future, based on specific cost and performance metrics.

9 Carbon nanotubes as charge acceptors

In addition to motivating their use as transparent conductors, the exceptionally high carrier mobilities in SWNTs make them good candidates for incorporation into the active layer of solar cells. High electron mobility, coupled with a long aspect ratio, has motivated the study of SWNTs as replacements for the fullerene electron accepting phase in polymer-based organic photovoltaic devices, Fig. 12a. A basic energy diagram for a polymer:SWNT bulk heterojunction active layer is shown in Fig. 12b. Current generation is based upon dissociation of photogenerated excitons *via* interfacial charge transfer, and two charge transfer processes are possible at the interface: (1) electron transfer from the LUMO of the photoexcited polymer (donor) to the LUMO of the SWNT (acceptor), and (2) hole transfer from the HOMO of the photoexcited SWNT to the HOMO of the polymer. In each case, the driving force for interfacial charge transfer is based upon the free energy change (ΔG) associated with dissociation of the exciton into free charges, and is defined as:

$$\vec{\Delta}G = |IP_D - EA_A| - E^{exciton}, \quad (5)$$

Here, IP_D is the ionization potential of the donor, EA_A is the electron affinity of the acceptor, and $E^{exciton}$ is the exciton energy (optical band gap) of the excited species (donor or acceptor), which is related to the electronic band gap, $E^{elec.}$, through the exciton binding energy (E_b): $E^{elec.} = E^{exciton} + E_b$.[191] Eqn (3) can be used to calculate the driving force for either electron or hole transfer, by using the exciton energy for the donor ($E_D^{exciton}$) or acceptor ($E_A^{exciton}$), respectively.

Despite the fact that this particular application has received a great deal of attention in the literature, the efficiencies of polymer:SWNT bulk heterojunction OPV cells have remained low. A number of fundamental studies in recent years have helped to elucidate several important aspects of these next-generation OPV active layers, and subsequent device studies have shown improved efficiencies. We have used time-resolved microwave conductivity (TRMC) to probe free charge carrier generation in SWNT:polymer active layers, using SWNTs with an average diameter $\langle d \rangle$ of 1.3 nm prepared by laser vaporization (LV) and the prototypical semiconducting polymer poly[3-hexylthiophene] (P3HT).[7,192] TRMC probes the yield and lifetime of

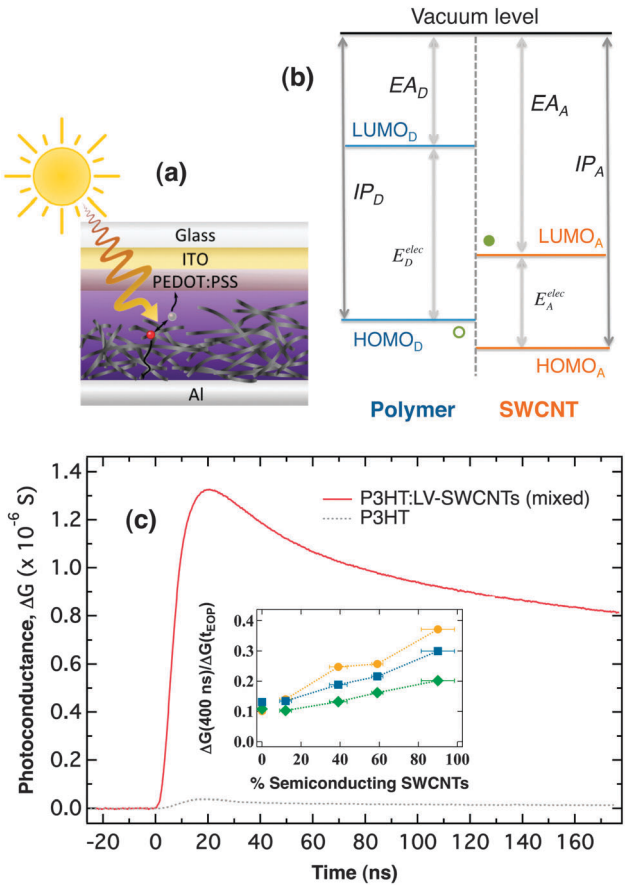

Fig. 12 (a) Schematic of a polymer:SWNT bulk heterojunction solar cell. (b) Simplified energy band diagram for polymer:SWNT solar cell. Exciton dissociation can occur through electron transfer from polymer to SWNT or through hole transfer from SWNT to polymer, if a sufficient energetic driving force exists (see text). The charge separated state in both cases consists of an electron in the acceptor LUMO and a hole in the donor HOMO, as shown in the figure as green filled and unfilled circles. (c) Photoconductance (ΔG) transients measured for P3HT with (red solid trace) or without (gray dashed trace) LV SWNTs ($\langle d \rangle \approx$ 1.3 nm). Inset shows the photoconductance signal measured at 400 ns, normalized to the end-of-pulse photoconductance signal, as a function of the percentage of semiconducting SWNTs in a P3HT:SWNT blend. The increase of this ratio with increasing semiconducting SWNT percentage indicates longer lifetimes for semiconducting-enriched blends. The photon flux for the transients shown is 2×10^{15} cm^{-2}, and for the inset it is 3×10^{13}, 2×10^{14}, and 1×10^{15} for the orange circles, blue squares, and green diamonds, respectively.

photogenerated charges through the intensity and time-dependent decay (respectively) of the photoinduced microwave absorbance of free and mobile charge carriers. Upon photoexcitation of P3HT in a SWNT:polymer blend at 532 nm, a strong long-lived microwave absorbance was observed, indicative of interfacial charge separation *via* electron transfer from P3HT to SWNTs, Fig. 12c. This result demonstrated that SWNT acceptors establish a sufficient driving force for interfacial electron transfer from typical semiconducting polymers, and that the resulting charge-separated state survives for microseconds (unpublished data). A follow-up study attempted to address the heterogeneity of electronic structure typically present in as-produced SWNT samples.[7] In particular, the lack of a bandgap in metallic SWNTs suggests that these SWNTs may act as efficient recombination centers in PV active layers. The authors separated metallic and semiconducting SWNTs by density gradient ultracentrifugation and formulated SWNT:P3HT blends with varying proportions of metallic and semiconducting SWNTs. Using TRMC as a probe, the authors found that the yield and lifetime of separated charge carriers systematically increased as the proportion of semiconducting SWNTs was increased within the blend. These results indicated that metallic SWNTs facilitate recombination, limit the efficiency of SWNT active layers, and should be quantitatively removed for optimization of SWNT photovoltaics. Fortunately, a number of routes exist for selective dispersion of semiconducting SWNTs in organic solvents, either *via* light-harvesting thiophene polymers analogous to P3HT[193] or *via* fluorene-based UV-absorbing polymers, which can be subsequently replaced with other polymers more suitable for OPV active layers.[194]

Moving forward, there are a number of challenges that remain for utilizing SWNT acceptors in OPV active layers. We suggest that one particularly important topic involves a better understanding of the role of the SWNT diameter in defining the energetic driving force for interfacial charge transfer. Spectroscopic studies have demonstrated that photoexcitation of P3HT in a SWNT:P3HT active layer produces a long-lived charge-separated state for SWNTs with $\langle d \rangle \approx 1.3$ nm[7,192] and $\langle d \rangle \approx 0.8$ nm.[195] Although some studies[18,195] suggest that a Type II band gap is only formed with P3HT for SWNTs $< \sim 1$ nm in diameter, a recent device study demonstrating the most efficient SWNT:P3HT active layers to date utilized semiconducting-enriched SWNTs with diameters up to 1.4 nm.[23] It is expected that the driving force for hole transfer will decrease with increasing SWNT diameter, and above a critical diameter such charge transfer will not be energetically favorable.[192] However, the driving force for electron transfer in these blends will always be rather large (>1 eV), based on the large difference in electron affinities for typical semiconducting polymers and semiconducting SWNTs. The question then becomes whether or not the hole remaining on the photoexcited polymer remains confined to the polymer or if it can be facilely transferred to the SWNT due the lack of a thermodynamic barrier (*e.g.* type-I band offset). Thus, spectroscopic[7,192] and device[23] investigations on SWNTs with diameters in the range of 1.3 to 1.4 nm suggest that if these nanotubes do indeed form Type I heterojunctions with polymers such as P3HT, then a kinetic barrier may hinder recombination and allow for long-lived charge separation and useful photovoltaic devices. Attempts to resolve the role of SWNT diameter in these OPV active layers will certainly facilitate the production of better devices in the future.

10 Active layer single-walled carbon nanotube heterostructures

The application of semiconducting carbon nanotubes as the light absorbing components of photovoltaic solar cells is motivated by the strong and tunable light absorbing characteristics

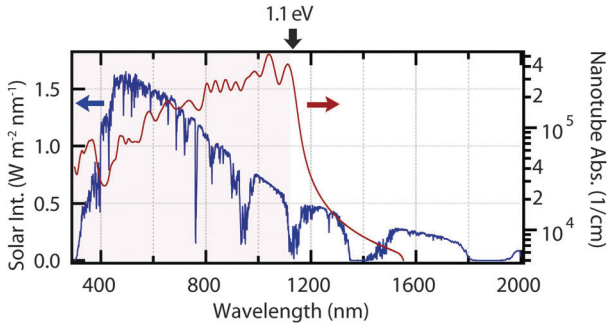

Fig. 13 Modeled absorption spectrum of a polydisperse mixture of nanotubes.

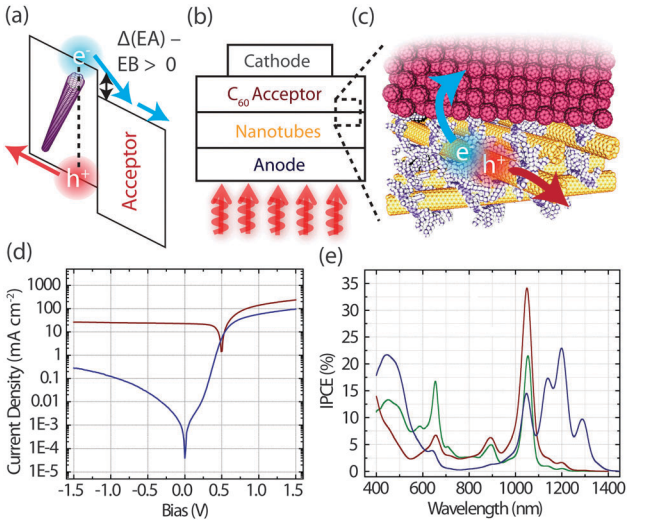

Fig. 14 (a) Energy levels of a type-II donor–acceptor heterojunction for driving electron-transfer. (b and c) Architecture of a nanotube–C_{60} bilayer planar heterojunction device. (d) Absolute current density *versus* bias for highly monodisperse (7,5)–C_{60} heterojunction device in the dark and under 100 mW cm^{-2} monochromatic illumination at 1053 nm, adapted from Bindl *et al.*[104] (e) IPCE *versus* wavelength. Blue curve for polydisperse mixture of nanotubes, adapted from Bindl *et al.*[25] Red and green curves for highly monodisperse (7,5) nanotubes, adapted from Bindl *et al.*[104]

of these materials. The optical responses of isolated (unbundled) semiconducting carbon nanotubes are dominated by excitons, which is to say that photogenerated electron–hole pairs in these materials are bound to each other with a binding energy, ε_B, that exceeds k_BT at room temperature.[37,73,77,88,174,196–200] The absorption coefficient of a neat film of monodisperse nanotubes is dye-like in strength,[16] remarkably exceeding 10^6 cm^{-1} and 5×10^5 cm^{-1}, at peak, in the near-infrared and visible spectra, respectively.

The peak optical absorption coefficient of a hypothetical neat film of nanotubes comprising a mixture of 10 different (n,m) species within this range is shown in Fig. 13. The peak absorption coefficient in the near-infrared even in this diluted mixture still exceeds $>10^5$ cm^{-1}, comparable to strongly absorbing dyes, semiconducting polymers, and direct-gap inorganic semiconductors. Over 86% of the AM1.5G solar photon flux for $h\nu > 1.1$ eV would be captured by a film of these nanotubes that is only 150 nm in thickness. Thus, in addition to their exceptional charge transport characteristics and potentially excellent photostability,[201–205] nanotubes are also incredibly efficient light-absorbers with nearly ideal bandgaps for capturing solar radiation.

The first challenge in employing nanotubes as the light absorbing components of photovoltaic devices is overcoming the exciton binding energy, ε_B, which is expected to be roughly 0.25 eV for a semiconducting nanotube of optical bandgap S_1 = 1.1 eV in an effective dielectric medium of $\kappa = 5$.[18,22] It has been previously discovered that excitons can be efficiently dissociated in single nanotube p–n junctions and field-effect transistor devices, due to the large electric-field at the Schottky contacts of these devices.[163,164,200,206–208] However, the scaling of this lateral nanoscale device architecture to macroscopic applications has not yet been demonstrated and it may not translate well to vertical device stacks, which are the preferred motif for most large-area optoelectronics applications.

An alternative approach for separating excitons into free charged carriers is to employ a type-II donor–acceptor heterojunction in which energy band offsets at the heterointerface between the donor nanotubes and a complementary hole or electron acceptor exceed ε_B, driving the spontaneous transfer of one polarity of charge from the nanotube to the acceptor, Fig. 14a–c. The donor–acceptor heterojunction strategy is similar to the approach employed in polymer photovoltaic devices[209–211] and scales easily to macroscopic large-area applications. The dissociation of excitons using the donor–acceptor heterojunction strategy is distinct from the approach demonstrated in Section 7 and in Fig. 10 in that an external bias is not needed to drive dissociation. This distinction is important because a solar cell operates in the fourth quadrant of a current–voltage plot in which free carriers must be spontaneously generated from excitons to drive a positive photovoltage and a reverse bias cannot be applied.

Carbon nanotube–acceptor type-II heterojunctions that show a photoresponse from the nanotubes have been successfully realized by several groups using a variety of charge accepting materials. Specifically, it has been shown that materials including C_{60}-fullerenes[17,18,20–22,25,104,143,212] and Si-nanocrystals[24] have the proper energetics for extracting photogenerated electrons from optically excited nanotubes, while polymers including poly(3-hexylthiophene) (P3HT) and P3HT-derivatives[18,213–215] and other carbon-based materials[23,216–219] have the proper energetics for extracting photogenerated holes. Evidence for the formation of a type-II heterojunction and for the dissociation of photogenerated excitons into separable charges has been gathered both spectroscopically and by fabricating heterojunction diode photovoltaic devices. Using devices, Bindl *et al.* have shown an absorbed-photon to collected-electron conversion efficiency (APCE) of >80% at optical transitions of nanotubes in planar bilayer heterojunction devices with an architecture of: an indium tin oxide (ITO) coated glass transparent anode/a thin film of type-controlled semiconducting nanotubes/a thin film of C_{60} between 50 and 120 nm in thickness, 10 nm of a cathode buffer bathocuproine (BCP)

and 100 nm of an Ag cathode, Fig. 14b.[22,104] In studies of nearly monodisperse (7,5) nanotubes dispersed by poly(fluorene) derivatives in heterojunctions with C_{60}, the APCE at the S_1 transition at 1050 nm, at the D mode phonon-allowed E symmetry exciton at 900 nm,[86] and at the S_2 transition at 650 nm, are 84% ± 7%, 85% ± 5%, and 84% ± 14%, respectively.

In general, in a bilayer planar heterojunction device, the APCE = $\eta_{ED}\eta_{CS}\eta_{CC}$, where η_{ED} is the exciton diffusion efficiency quantifying the fraction of excitons that are photogenerated that diffuse to the heterointerface, η_{CS} is the charge separation efficiency quantifying the fraction of excitons which have already reached the heterointerface, which then dissociate into separable electrons and holes, and η_{CC} is the charge collection efficiency quantifying the fraction of already separated electron–hole pairs that are collected at the contacts. Experimentally, the APCE of >80% in the thin limit of <5 layers of nanotubes implies that each of η_{ED}, η_{CS}, and η_{CC} are >80%. The most important factor in evaluating C_{60} as an electron acceptor is η_{CS}. The η_{CS} is >80% for nanotubes of diameter <1 nm (S_1 > 1 eV) and falls off for nanotubes of diameter >1 nm and S_1 < 1 eV.[22] As the bandgap of a nanotube decreases, the driving force for electron separation at a heterointerface between that nanotube and C_{60} will decrease and eventually invert as the electron affinity of the nanotube approaches the workfunction of graphite at ≈4.5 eV, Fig. 14a. The data imply that this inversion occurs for nanotubes of $S_1 \approx 1$ eV.

The high η_{CS} is an impressive and interesting result, both scientifically and technologically. Scientifically, the high η_{CS} is interesting because (i) it is significantly higher than the typically observed quantum yield for light emission from semiconducting nanotubes (<10%); (ii) it indicates that both dark and bright excitons (optically and non-optically allowed excitons, respectively) are dissociated; and (iii) it suggests that the rate for exciton dissociation is very fast, much faster than the rate for non-radiative recombination of excitons $(10\ ps)^{-1}$.[220–224] Technologically, this finding indicates that C_{60} is an excellent choice as an acceptor for nanotubes of S_1 > 1.0 eV and furthermore that high-efficiency carbon nanotube-based photovoltaic devices and photodetectors are possible based on the all-carbon nanotube–C_{60} material pair.

Further evidence that C_{60} is an appropriate acceptor for small diameter semiconducting nanotubes is apparent in the measured current–voltage characteristics of the heterojunctions. In the dark (blue curve in Fig. 14d), the current–voltage characteristics are diode-like, as expected for a type-II heterojunction, with a rectification ratio >400 at ±1 V. Under illumination (red curve in Fig. 14d), a photovoltaic effect is observed, with a short-circuit current at zero-bias and an open-circuit voltage at zero-current. Power conversion is driven everywhere in the 4th quadrant of the current–voltage characteristics, demonstrating the conversion of the potential energy stored in photogenerated excitons into electrical energy.

The challenge moving forward is to implement the SWNT–C_{60} or similar nanotube–acceptor material pairs in solar cell devices with high power conversion efficiency. The power conversion efficiency of a photovoltaic device depends on the product of current generation and voltage. The voltage is mostly determined by the energy levels of the nanotubes and the acceptor, in addition to recombination rates. The current generation is determined by the integration over photon energy of the product of the incident solar flux and the incident-photon to collected-electron conversion efficiency (IPCE), where the IPCE = η_AAPCE and η_A is the fraction of incident photons that are absorbed by the solar cell at a particular photon energy. To achieve a high broadband IPCE, the photoabsorbing materials must be implemented in films of thickness on the order of the broadband absorption length, which would be 150 nm for the hypothetical mixture of nanotubes discussed above. The high IPCE must be achieved without sacrificing the high η_{ED}, η_{CS}, and η_{CC}.

One hope is that it will be eventually possible to exploit the exceptionally long diffusion length of excitons along the length of individual nanotubes (potentially as long as 600 nm[149,225,226] compared with 5–15 nm in molecules and polymers[227–231]) to create high-efficiency planar bilayer heterojunction devices from films of standing-up nanotubes over-coated by a layer of C_{60}. Excitons photogenerated in films of the standing-up nanotubes would rapidly diffuse along the length of the individual nanotubes to the SWNT/C_{60} interface where they would dissociate into free charged carriers and then separate, Fig. 15a. Problematically, however, the growth or assembly of densely packed, oriented semiconducting nanotubes has not yet been achieved.

Bindl *et al.* have explored planar bilayer nanotube–C_{60} heterojunction devices as a means for characterizing exciton diffusion in solution-deposited films of nanotubes, in which the nanotubes have the opposite morphology and are lying down on the substrate with their long-axis perpendicular to the device-axis (*e.g.* not oriented towards the C_{60}) as a result of surface tension effects during drying.[22,25] The authors have found that, in this case, the exciton diffusion length towards the C_{60} is limited to ~5–10 nm by poor inter-nanotube coupling. A 10 nm diffusion length could be sufficient for monochromatic power conversion applications, using monodisperse nanotubes with an absorption-length of ~10 nm. However, this diffusion length is insufficient for high-efficiency broadband solar light conversion. The IPCEs of a planar bilayer heterojunction built from films of lying-down nanotubes of various

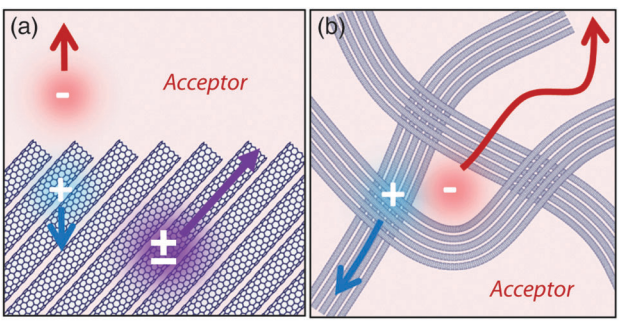

Fig. 15 (a) Ideal standing-up bilayer SWNT–acceptor heterojunction morphology. (b) Ideal blended SWNT–acceptor heterojunction morphology.

bandgap distributions are shown in Fig. 14e. Using a nanotube film comprised of a mixture of the (7,5), (7,6), (8,6), (8,7), and (9,7) chiralities with S_1 transitions ranging from 1050–1330 nm (blue curve in Fig. 14e), the sub-10 nm inter-nanotube diffusion-length specifically limits the IPCE at the S_1 transitions to 20%. The IPCE can be increased by tuning the composition. For example, using highly monochiral (7,5) tubes, the IPCE increases to $\sim$35% at the S_1 transition at 1050 nm (red curve in Fig. 14e). The IPCE in the visible spectrum can be increased by decreasing the thickness of the C_{60} layer, which also acts as an optical spacer that affects optical interference effects in the device stack (green curve in Fig. 14e). The current–voltage characteristics of a highly monochiral (7,5)/C_{60} heterointerface under 1053 nm monochromatic excitation at an intensity of 100 mW cm^{-2} are shown in Fig. 14d. A monochromatic short-circuit current density of 23 mA cm^{-2}, an open-circuit voltage of 492 meV, and a fill-factor of 0.62 are observed, yielding a monochromatic power conversion efficiency of 7.1%. The efficiency under the solar spectrum would still be expected to be $<$1% due to the fact that the absorption length in between the S_1 and S_2 transitions is much longer than the exciton diffusion length of 5–10 nm.

Our most significant accomplishment to date is that we have shown that photogenerated excitons can be efficiency dissociated into separable charge at nanotube–acceptor heterojunctions (high η_{CS}). Looking forward, the route to high efficiency is to next improve η_{ED}. As previously mentioned, learning how to assemble densely packed films of oriented, standing-up semiconducting nanotubes would overcome the problem of poor inter-nanotube diffusion, increase η_{ED}, and therefore enable high-efficiency nanotube–C_{60} heterojunction devices in the bilayer architecture, Fig. 15a. η_{ED} can potentially be further improved by preparing devices from more homo-chiral samples with improved inter-nanotube coupling, where exciton transport seems to be coherent in between tubes.[78]

An alternative approach for overcoming poor inter-nanotube exciton migration is to mix semiconducting nanotubes directly with electron acceptors in blended films. A blend potentially overcomes the exciton-diffusion limitations of bilayer architectures by always establishing the nanotube light absorbing components in close proximity to the acceptors. In a preliminary attempt, Bindl *et al.* have investigated charge generation in semiconducting SWNT–C_{60}-fullerene derivative blends, albeit with mild success.[21]

The ideal morphology of a blend is to achieve a controlled phase separation between the donor and fullerenes at a length scale on the order of the exciton diffusion length $\sim$10 nm, Fig. 15b. In contrast, the solution casting of SWNT–C_{60} derivative mixtures produces blends in which the nanotubes and fullerene-derivatives are finely inter-dispersed with little phase separation between the two components. The impact of the overly fine dispersion is excessive surface area for charge recombination, which limits the peak IPCE at the S_1 transitions from 1050–1350 nm to $\sim$18%.[21] Promising alternative options for achieving more ideal phase separation are to pre-group nanotubes in solution in bundles of diameter $\sim$10 nm prior to blending with electron acceptors; or to first fabricate porous nanotube networks with controlled pore size and then subsequently back-fill the pores with electron acceptors.

Blended heterojunctions are the preferred device architecture in polymer solar cells due to a similarly short exciton diffusion length-scale. Polymer–fullerene blends have the advantage, however, of undergoing a natural phase separation after film-casting and in some cases after annealing, enabling more facile optimization of the nanostructure of the blends.[209–211] In contrast, the morphology of the nanotube–fullerene blends is more invariant upon annealing due to nanotubes' stiffness and size. Thus, the most substantial roadblock currently limiting the development of high-efficiency SWNT–acceptor heterojunction solar cells in both bilayer planar and blended architectures is controlling the morphology of the nanotubes. Their large unit cells, built-in crystallinity, long length, and rigidity give rise to new challenges unique to polymers. The same attributes, however, are also responsible for nanotubes' exceptional properties including their optical bandgaps that are easily tunable throughout the near-infrared, their superior charge and exciton transport characteristics, and their excellent photostability. Thus, there is good reason to learn new approaches for controlling the morphology of nanotubes in films and blends. Success in these endeavors promises to result in new classes of polymer-like solar cells fabricated using next-generation, crystalline, high-performance nanotubes as polymer replacements.

11 Conclusion

We have reviewed important photophysical processes for the integration of SWNTs into photovoltaic devices and presented recent device results with a perspective of using these fascinating and versatile materials for solar energy conversion. Strong light absorption, efficient energy transport, and the promise of the efficient generation of charges make SWNTs an outstanding candidate material for active layers in photovoltaics. Bulk-heterojunction or bi-layer device design can take advantage of these properties and leave plenty of room for optimizing light absorption and charge generation. Besides active layers, SWNTs as thin film conductors make the possibility of constructing all carbon solar cells consisting of junctions of p-doped–intrinsic–n-doped (pin-junctions) carbon nanomaterials. The future is bright for nanotubes in the field of photovoltaics, and as sample quality continues to increase new discoveries will lead to new milestones in the development of SWNTs for solar energy conversion applications.

Acknowledgements

MSA acknowledges support from the Air Force Office of Scientific Research (FA9550-12-1-0063), the National Science Foundation through the University of Wisconsin-Madison Center of Excellence for Materials Research and Innovation (DMR-1121288), the National Science Foundation (DMR-0905861), the U.S. Army Research Office (W911NF-12-1-0025), and a 3M Non-Tenured

Faculty Grant. JLB graciously acknowledges funding from the Solar Photochemistry program of the U.S. Department of Energy, Office of Sciences, Division of Chemical Sciences, Geosciences and Biosciences, under Contract No. DE-AC36-08GO28308 to NREL. This work was performed, in part, at the Center for Integrated Nanotechnologies, a U.S. Department of Energy, Office of Basic Energy Sciences user facility and partially supported by the LANL LDRD program. Los Alamos National Laboratory is operated by Los Alamos National Security, LLC, for the National Nuclear Security Administration of the U.S. Department of Energy under contract DE-AC52-06NA25396.

References

1 *Carbon nanotubes: advanced topics in the synthesis, structure, properties and applications*, ed. M. Jorio, A. Dresselhaus and G. Dresselhaus, Springer, Berlin, 2008.
2 R. B. Weisman and S. M. Bachilo, *Nano Lett.*, 2003, **3**, 1235–1238.
3 R. C. Tenent, T. M. Barnes, J. D. Bergeson, A. J. Ferguson, B. To, L. M. Gedvilas, M. J. Heben and J. L. Blackburn, *Adv. Mater.*, 2009, **21**, 3210–3216.
4 M. J. O'Connell, E. E. Eibergen and S. K. Doorn, *Nat. Mater.*, 2005, **4**, 412–418.
5 J. J. Crochet, S. Hoseinkhani, L. Lüer, T. Hertel, S. K. Doorn and G. Lanzani, *Phys. Rev. Lett.*, 2011, **107**, 257402.
6 M.-H. Ham, G. L. C. Paulus, C. Y. Lee, C. Song, K. Kalantarzadeh, W. Choi, J.-H. Han and M. S. Strano, *ACS Nano*, 2010, **4**, 6251–6259.
7 J. M. Holt, A. J. Ferguson, N. Kopidakis, B. A. Larsen, J. Bult, G. Rumbles and J. L. Blackburn, *Nano Lett.*, 2010, **10**, 4627–4633.
8 X. Dang, H. Yi, M.-H. Ham, J. Qi, D. S. Yun, R. Ladewski, M. S. Strano, P. T. Hammond and A. M. Belcher, *Nat. Nanotechnol.*, 2011, **6**, 377–384.
9 M. M. Stylianakis and E. Kymakis, *Appl. Phys. Lett.*, 2012, **100**, 093301.
10 A. J. Ferguson, J. L. Blackburn, J. M. Holt, N. Kopidakis, R. C. Tenent, T. M. Barnes, M. J. Heben and G. Rumbles, *J. Phys. Chem. Lett.*, 2010, **1**, 2406–2411.
11 A. Javey, H. Kim, M. Brink, Q. Wang, A. Ural, J. Guo, P. McIntyre, P. McEuen, M. Lundstrom and H. Dai, *Nat. Mater.*, 2002, **1**, 241–246.
12 T. Dürkop, S. A. Getty, E. Cobas and M. S. Fuhrer, *Nano Lett.*, 2004, **4**, 35–39.
13 M. O'Connell, S. Bachilo, C. Huffman, V. Moore, M. Strano, E. Haroz, K. Rialon, P. Boul, W. Noon, C. Kittrell, J. Ma, R. Hauge, R. Weisman and R. Smalley, *Science*, 2002, **297**, 593–596.
14 S. M. Bachilo, M. S. Strano, C. Kittrell, R. H. Hauge, R. E. Smalley and R. B. Weisman, *Science*, 2002, **298**, 2361–2366.
15 M. S. Arnold, J. E. Sharping, S. I. Stupp, P. Kumar and M. C. Hersam, *Nano Lett.*, 2003, **3**, 1549–1554.
16 F. Schöppler, C. Mann, T. C. Hain, F. M. Neubauer, G. Privitera, F. Bonaccorso, D. Chu, A. C. Ferrari and T. Hertel, *J. Phys. Chem. C*, 2011, **115**, 14682–14686.
17 M. S. Arnold, J. D. Zimmerman, C. K. Renshaw, X. Xu, R. R. Lunt, C. M. Austin and S. R. Forrest, *Nano Lett.*, 2009, **9**, 3354–3358.
18 D. J. Bindl, N. S. Safron and M. S. Arnold, *ACS Nano*, 2010, **4**, 5657–5664.
19 F. A. Lemasson, T. Strunk, P. Gerstel, F. Hennrich, S. Lebedkin, C. Barner-Kowollik, W. Wenzel, M. M. Kappes and M. Mayor, *J. Am. Chem. Soc.*, 2011, **133**, 652–655.
20 D. J. Bindl and M. S. Arnold, *Int. J. High Speed Electron. Syst.*, 2011, **20**, 687–695.
21 D. Bindl, A. Brewer and M. Arnold, *Nano Res.*, 2011, **4**, 1174–1179.
22 D. J. Bindl, M.-Y. Wu, F. C. Prehn and M. S. Arnold, *Nano Lett.*, 2011, **11**, 455–460.
23 S. Ren, M. Bernardi, R. R. Lunt, V. Bulovic, J. C. Grossman and S. Gradeak, *Nano Lett.*, 2011, **11**, 5316–5321.
24 V. Švrček, S. Cook, S. Kazaoui and M. Kondo, *J. Phys. Chem. Lett.*, 2011, **2**, 1646–1650.
25 D. Bindl and M. Arnold, *Chem. Phys.*, 2013, **413**, 29–34.
26 M. Zheng, A. Jagota, M. S. Strano, A. P. Santos, P. Barone, S. G. Chou, B. A. Diner, M. S. Dresselhaus, R. S. Mclean, G. B. Onoa, G. G. Samsonidze, E. D. Semke, M. Usrey and D. J. Walls, *Science*, 2003, **302**, 1545–1548.
27 M. S. Arnold, S. I. Stupp and M. C. Hersam, *Nano Lett.*, 2005, **5**, 713–718.
28 M. S. Arnold, S. I. Stupp and M. C. Hersam, *ASME Conf. Proc.*, 2006, **2006**, 373–380.
29 M. S. Arnold, *Doctoral Thesis: Photophysics, Biofunctionalization, and Sorting via Density Differentiation*, Northwestern University, 2006.
30 M. S. Arnold, A. A. Green, J. F. Hulvat, S. I. Stupp and M. C. Hersam, *Nat. Nanotechnol.*, 2006, **1**, 60–65.
31 A. Nish, J.-Y. Hwang, J. Doig and R. J. Nicholas, *Nat. Nanotechnol.*, 2007, **2**, 640–646.
32 M. S. Arnold, J. Suntivich, S. I. Stupp and M. C. Hersam, *ACS Nano*, 2008, **2**, 2291–2300.
33 X. Tu, S. Manohar, A. Jagota and M. Zheng, *Nature*, 2009, **460**, 250–253.
34 S. Ghosh, S. M. Bachilo and R. B. Weisman, *Nat. Nanotechnol.*, 2010, **5**, 443–450.
35 H. Liu, D. Nishide, T. Tanaka and H. Kataura, *Nat. Commun.*, 2011, **2**, 1–8.
36 J. J. Crochet, *Doctoral Thesis: Charge and Energy Transfer Dynamics in Single-Wall Carbon Nanotube Ensembles*, Vanderbilt University, 2007.
37 F. Wang, G. Dukovic, L. E. Brus and T. F. Heinz, *Science*, 2005, **308**, 838–841.
38 C. Voisin, S. Berger, S. Berciaud, H. Yan, J.-S. Lauret, G. Cassabois, P. Roussignol, J. Hone and T. F. Heinz, *Phys. Status Solidi B*, 2012, **249**, 900–906.
39 A. J. Siitonen, D. A. Tsyboulski, S. M. Bachilo and R. B. Weisman, *J. Phys. Chem. Lett.*, 2010, **1**, 2189–2192.
40 A. J. Siitonen, S. M. Bachilo, D. A. Tsyboulski and R. B. Weisman, *Nano Lett.*, 2012, **12**, 33–38.
41 C. Sciascia, J. Crochet, T. Hertel and G. Lanzani, *Eur. Phys. J. B*, 2010, **75**, 115–120.

42 J. Park, P. Deria and M. J. Therien, *J. Am. Chem. Soc.*, 2011, **133**, 17156–17159.
43 A. V. Naumov, S. Ghosh, D. A. Tsyboulski, S. M. Bachilo and R. B. Weisman, *ACS Nano*, 2011, **5**, 1639–1648.
44 L. Lüer, J. Crochet, T. Hertel, G. Cerullo and G. Lanzani, *ACS Nano*, 2010, **4**, 4265–4273.
45 T. Hertel, S. Himmelein, T. Ackermann, D. Stich and J. Crochet, *ACS Nano*, 2010, **4**, 7161–7168.
46 F. Hennrich, M. M. Kappes, M. Klinger and A.-N. Unterreiner, *J. Phys. Chem. C*, 2011, **115**, 23711–23717.
47 E. H. Hároz, J. G. Duque, W. D. Rice, C. G. Densmore, J. Kono and S. K. Doorn, *Phys. Rev. B: Condens. Matter Mater. Phys.*, 2011, **84**, 121403.
48 M. W. Graham, Y.-Z. Ma, A. A. Green, M. C. Hersam and G. R. Fleming, *J. Chem. Phys.*, 2011, **134**, 034504.
49 S. Ghosh, S. M. Bachilo, R. A. Simonette, K. M. Beckingham and R. B. Weisman, *Science*, 2010, **330**, 1656–1659.
50 J. Gao and M. A. Loi, *Eur. Phys. J. B*, 2010, **75**, 121–126.
51 T. K. Cherukuri, D. A. Tsyboulski and R. B. Weisman, *ACS Nano*, 2012, **6**, 843–850.
52 P. Araujo, P. Pesce, M. Dresselhaus, K. Sato, R. Saito and A. Jorio, *Physica E*, 2010, **42**, 1251–1261.
53 J. Jiang, R. Saito, G. G. Samsonidze, A. Jorio, S. G. Chou, G. Dresselhaus and M. S. Dresselhaus, *Phys. Rev. B: Condens. Matter Mater. Phys.*, 2007, **75**, 035407.
54 J. G. Duque, H. Chen, A. K. Swan, A. P. Shreve, S. Kilina, S. Tretiak, X. Tu, M. Zheng and S. K. Doorn, *ACS Nano*, 2011, **5**, 5233–5241.
55 M. Machón, S. Reich, H. Telg, J. Maultzsch, P. Ordejón and C. Thomsen, *Phys. Rev. B: Condens. Matter Mater. Phys.*, 2005, **71**, 035416.
56 S. V. Goupalov, B. C. Satishkumar and S. K. Doorn, *Phys. Rev. B: Condens. Matter Mater. Phys.*, 2006, **73**, 115401.
57 J. Jiang, R. Saito, K. Sato, J. S. Park, G. G. Samsonidze, A. Jorio, G. Dresselhaus and M. S. Dresselhaus, *Phys. Rev. B: Condens. Matter Mater. Phys.*, 2007, **75**, 035405.
58 H. Telg, C. Thomsen and J. Maultzsch, *J. Nanophotonics*, 2010, **4**, 041660.
59 H. Telg, J. Maultzsch, S. Reich, F. Hennrich and C. Thomsen, *Phys. Rev. Lett.*, 2004, **93**, 177401.
60 C. Fantini, A. Jorio, M. Souza, M. Strano, M. Dresselhaus and M. Pimenta, *Phys. Rev. Lett.*, 2004, **93**, 147406.
61 S. K. Doorn, D. A. Heller, P. W. Barone, M. L. Usrey and M. S. Strano, *Appl. Phys. A: Mater. Sci. Process.*, 2004, **78**, 1147–1155.
62 J. Maultzsch, H. Telg, S. Reich and C. Thomsen, *Phys. Rev. B: Condens. Matter Mater. Phys.*, 2005, **72**, 205438.
63 H. Telg, J. G. Duque, M. Staiger, X. Tu, F. Hennrich, M. M. Kappes, M. Zheng, J. Maultzsch, C. Thomsen and S. K. Doorn, *ACS Nano*, 2012, **6**, 904–911.
64 M. Gao, J. M. Zuo, R. D. Twesten, I. Petrov, L. a. Nagahara and R. Zhang, *Appl. Phys. Lett.*, 2003, **82**, 2703.
65 T. W. Odom and J.-l. Huang, *Nature*, 1998, **391**, 1997–1999.
66 H. Htoon, M. J. O'Connell, P. J. Cox, S. K. Doorn and V. I. Klimov, *Phys. Rev. Lett.*, 2004, **93**, 1–4.
67 M. Fouquet, H. Telg, J. Maultzsch, Y. Wu, B. Chandra, J. Hone, T. Heinz and C. Thomsen, *Phys. Rev. Lett.*, 2009, **102**, 075501.
68 H. Kataura, Y. Kumazawa, Y. Maniwa, I. Umezu, S. Suzuki, Y. Ohtsuka and Y. Achiba, *Synth. Met.*, 1999, **103**, 2555–2558.
69 V. N. Popov, L. Henrard and P. Lambin, *Nano Lett.*, 2004, **4**, 1795–1799.
70 E. Chang, G. Bussi, A. Ruini and E. Molinari, *Phys. Rev. Lett.*, 2004, **92**, 1–4.
71 V. Perebeinos, J. Tersoff and P. Avouris, *Phys. Rev. Lett.*, 2004, **92**, 257402.
72 C. Spataru, S. Ismail-Beigi, L. Benedict and S. Louie, *Phys. Rev. Lett.*, 2004, **92**, 77402.
73 J. Maultzsch, R. Pomraenke, S. Reich, E. Chang, D. Prezzi, a. Ruini, E. Molinari, M. Strano, C. Thomsen and C. Lienau, *Phys. Rev. B: Condens. Matter Mater. Phys.*, 2005, **72**, 1–4.
74 F. Wang, D. Cho, B. Kessler, J. Deslippe, P. Schuck, S. Louie, A. Zettl, T. F. Heinz and Y. Shen, *Phys. Rev. Lett.*, 2007, **99**, 1–4.
75 S. K. Doorn, P. T. Araujo, K. Hata and A. Jorio, *Phys. Rev. B: Condens. Matter Mater. Phys.*, 2008, **78**, 165408.
76 C. D. Spataru, S. Ismail-Beigi, R. B. Capaz and S. G. Louie, *Phys. Rev. Lett.*, 2005, **95**, 247402.
77 T. Ando, *J. Phys. Soc. Jpn.*, 1997, **66**, 1066–1073.
78 J. J. Crochet, J. D. Sau, J. G. Duque, S. K. Doorn and M. L. Cohen, *ACS Nano*, 2011, **5**, 2611–2618.
79 P. May, H. Telg, G. Zhong, J. Robertson, C. Thomsen and J. Maultzsch, *Phys. Rev. B: Condens. Matter Mater. Phys.*, 2010, **82**, 1–6.
80 O. A. Dyatlova, J. Gomis-Bresco, E. Malic, H. Telg, J. Maultzsch, G. Zhong, J. Geng and U. Woggon, *Phys. Rev. B: Condens. Matter Mater. Phys.*, 2012, **85**, 245449.
81 L. Lüer, S. Hoseinkhani, D. Polli, J. Crochet, T. Hertel and G. Lanzani, *Nat. Phys.*, 2009, **5**, 54–58.
82 J. Deslippe, C. D. Spataru, D. Prendergast and S. G. Louie, *Nano Lett.*, 2007, **7**, 1626–1630.
83 T. Ando and S. Uryu, *Phys. Status Solidi C*, 2009, **6**, 173–180.
84 O. N. Torrens, M. Zheng and J. M. Kikkawa, *Phys. Rev. Lett.*, 2008, **101**, 157401.
85 P. M. Vora, X. Tu, E. J. Mele, M. Zheng and J. M. Kikkawa, *Phys. Rev. B: Condens. Matter Mater. Phys.*, 2010, **81**, 155123.
86 J. L. Blackburn, J. M. Holt, V. M. Irurzun, D. E. Resasco and G. Rumbles, *Nano Lett.*, 2012, **12**, 1398–1403.
87 F. Andrea, *Solid State Commun.*, 2007, **143**, 47–57.
88 V. Perebeinos, J. Tersoff and P. Avouris, *Nano Lett.*, 2005, **5**, 2495–2499.
89 R. M. Konik, *Phys. Rev. Lett.*, 2011, **106**, 136805.
90 C. L. Kane and E. J. Mele, *Phys. Rev. Lett.*, 2004, **93**, 197402.
91 A. Jorio, C. Fantini, M. A. Pimenta, R. B. Capaz, G. G. Samsonidze, G. Dresselhaus, M. S. Dresselhaus, J. Jiang, N. Kobayashi, A. Grüneis and R. Saito, *Phys. Rev. B: Condens. Matter Mater. Phys.*, 2005, **71**, 075401.
92 J. Shaver, S. A. Crooker, J. A. Fagan, E. K. Hobbie, N. Ubrig, O. Portugall, V. Perebeinos, P. Avouris and J. Kono, *Phys. Rev. B: Condens. Matter Mater. Phys.*, 2008, **78**, 081402.

93 A. Srivastava, H. Htoon, V. I. Klimov and J. Kono, *Phys. Rev. Lett.*, 2008, **101**, 087402.
94 R. Matsunaga, Y. Miyauchi, K. Matsuda and Y. Kanemitsu, *Phys. Rev. B: Condens. Matter Mater. Phys.*, 2009, **80**, 115436.
95 J. G. Duque, C. E. Hamilton, G. Gupta, S. A. Crooker, J. J. Crochet, A. Mohite, H. Htoon, K. A. D. Obrey, A. M. Dattelbaum and S. K. Doorn, *ACS Nano*, 2011, **5**, 6686–6694.
96 J. J. Crochet, J. G. Duque, J. H. Werner, B. Lounis, L. Cognet and S. K. Doorn, *Nano Lett.*, 2012, **12**, 5091–5096.
97 R. B. Capaz, C. D. Spataru, S. Ismail-Beigi and S. G. Louie, *Phys. Rev. B: Condens. Matter Mater. Phys.*, 2006, **74**, 121401.
98 S. Abe, M. Schreiber, W. P. Su and J. Yu, *Phys. Rev. B: Condens. Matter Mater. Phys.*, 1992, **45**, 9432–9435.
99 B. F. Habenicht and O. V. Prezhdo, *J. Am. Chem. Soc.*, 2012, **134**, 15648–15651.
100 J. Park, P. Deria and M. J. Therien, *J. Am. Chem. Soc.*, 2011, **133**, 17156–17159.
101 S. M. Santos, B. Yuma, S. Berciaud, J. Shaver, M. Gallart, P. Gilliot, L. Cognet and B. Lounis, *Phys. Rev. Lett.*, 2011, **107**, 187401.
102 J. S. Park, Y. Hirana, S. Mouri, Y. Miyauchi, N. Nakashima and K. Matsuda, *J. Am. Chem. Soc.*, 2012, **134**, 14461–14466.
103 B. O. Tayo and S. V. Rotkin, *Phys. Rev. B: Condens. Matter Mater. Phys.*, 2012, **86**, 125431.
104 D. J. Bindl and M. S. Arnold, *J. Phys. Chem. C*, 2013, **117**, 2390–2395.
105 P. T. Araujo, S. K. Doorn, S. Kilina, S. Tretiak, E. Einarsson, S. Maruyama, H. Chacham, M. A. Pimenta and A. Jorio, *Phys. Rev. Lett.*, 2007, **98**, 067401.
106 J. Crochet, M. Clemens and T. Hertel, *J. Am. Chem. Soc.*, 2007, **129**, 8058–8059.
107 T. Ebbesen and P. Ajayan, *Nature*, 1992, **358**, 220–222.
108 P. Nikolaev, M. J. Bronikowski, R. Bradley, F. Rohmund, D. T. Colbert, K. Smith and R. E. Smalley, *Chem. Phys. Lett.*, 1999, **313**, 91–97.
109 B. Kitiyanan, W. Alvarez, J. Harwell and D. Resasco, *Chem. Phys. Lett.*, 2000, **317**, 497–503.
110 A. Rinzler, J. Liu, H. Dai, P. Nikolaev, C. Huffman, F. Rodríguez-Macías, P. Boul, A. Lu, D. Heymann, D. Colbert, R. Lee, J. Fischer, A. Rao, P. Eklund and R. Smalley, *Appl. Phys. A: Mater. Sci. Process.*, 1998, **67**, 29–37.
111 H. Dumlich and S. Reich, *Phys. Rev. B: Condens. Matter Mater. Phys.*, 2011, **84**, 064121.
112 M. J. O'Connell, P. Boul, L. M. Ericson, C. Huffman, Y. Wang, E. Haroz, C. Kuper, J. Tour, K. D. Ausman and R. E. Smalley, *Chem. Phys. Lett.*, 2001, **342**, 265–271.
113 V. C. Moore, M. S. Strano, E. H. Haroz, R. H. Hauge and R. E. Smalley, *Nano Lett.*, 2003, **3**, 1379–1382.
114 J. G. Duque, A. N. G. Parra-Vasquez, N. Behabtu, M. J. Green, A. L. Higginbotham, B. K. Price, A. D. Leonard, H. K. Schmidt, B. Lounis, J. M. Tour, S. K. Doorn, L. Cognet and M. Pasquali, *ACS Nano*, 2010, **4**, 3063–3072.
115 J. G. Duque, C. G. Densmore and S. K. Doorn, *J. Am. Chem. Soc.*, 2010, **132**, 16165–16175.
116 M. Calvaresi, M. Dallavalle and F. Zerbetto, *Small*, 2009, **5**, 2191–2198.
117 S.-Y. Ju, W. P. Kopcha and F. Papadimitrakopoulos, *Science*, 2009, **323**, 1319–1323.
118 D. A. Tsyboulski, J.-D. R. Rocha, S. M. Bachilo, L. Cognet and R. B. Weisman, *Nano Lett.*, 2007, **7**, 3080–3085.
119 N. R. Tummala and A. Striolo, *ACS Nano*, 2009, **3**, 595–602.
120 R. K. Wang, W.-C. Chen, D. K. Campos and K. J. Ziegler, *J. Am. Chem. Soc.*, 2008, **130**, 16330–16337.
121 W. Wenseleers, I. Vlasov, E. Goovaerts, E. Obraztsova, A. Lobach and A. Bouwen, *Adv. Funct. Mater.*, 2004, **14**, 1105–1112.
122 S. Niyogi, S. Boukhalfa, S. B. Chikkannanavar, T. J. McDonald, M. J. Heben and S. K. Doorn, *J. Am. Chem. Soc.*, 2007, **129**, 1898–1899.
123 M. S. Strano, C. B. Huffman, V. C. Moore, M. J. O'Connell, E. H. Haroz, J. Hubbard, M. Miller, K. Rialon, C. Kittrell, S. Ramesh, R. H. Hauge and R. E. Smalley, *J. Phys. Chem. B*, 2003, **107**, 6979–6985.
124 R. Baughman, A. Zakhidov and W. de Heer, *Science*, 2002, **297**, 787–792.
125 H. Dai, *Surf. Sci.*, 2002, **500**, 218–241.
126 R. Wang, P. Cherukuri, J. G. Duque, T. K. Leeuw, M. K. Lackey, C. H. Moran, V. C. Moore, J. L. Conyers, R. E. Smalley, H. K. Schmidt, R. B. Weisman and P. S. Engel, *Carbon*, 2007, **45**, 2388–2393.
127 J. G. Duque, M. Pasquali and H. K. Schmidt, *J. Am. Chem. Soc.*, 2008, **130**, 15340–15347.
128 W.-C. Chen, R. K. Wang and K. J. Ziegler, *ACS Appl. Mater. Interfaces*, 2009, **1**, 1821–1826.
129 S. Niyogi, C. G. Densmore and S. K. Doorn, *J. Am. Chem. Soc.*, 2009, **131**, 1144–1153.
130 C. A. Silvera-Batista, P. Weinberg, J. E. Butler and K. J. Ziegler, *J. Am. Chem. Soc.*, 2009, **131**, 12721–12728.
131 X. Tu, A. R. H. Walker, C. Y. Khripin and M. Zheng, *J. Am. Chem. Soc.*, 2011, **133**, 12998–13001.
132 J. Crochet, M. Clemens and T. Hertel, *Phys. Status Solidi B*, 2007, **244**, 3964–3968.
133 A. A. Green and M. C. Hersam, *Adv. Mater.*, 2011, **23**, 2185–2190.
134 K. Yanagi, Y. Miyata and H. Kataura, *Appl. Phys. Express*, 2008, **1**, 4003.
135 P. Zhao, E. Einarrson, R. Xiang, Y. Murakami and S. Maruyama, *J. Phys. Chem. C*, 2010, **114**, 4831–4834.
136 K. Moshammer, F. Hennrich and M. Kappes, *Nano Res.*, 2009, **2**, 599–606.
137 K. Tvrdy, R. M. Jain, R. Han, A. J. Hilmer, T. P. McNicholas and M. S. Strano, *ACS Nano*, 2013, **7**, 1779–1789.
138 A. J. Blanch, J. S. Quinton and J. G. Shapter, *Carbon*, 2013, **60**, 471–480.
139 N. Stürzl, F. Hennrich, S. Lebedkin and M. M. Kappes, *J. Phys. Chem. C*, 2009, **113**, 14628–14632.
140 H. Ozawa, N. Ide, T. Fujigaya, Y. Niidome and N. Nakashima, *Chem. Lett.*, 2011, 239–241.
141 A. A. Green and M. C. Hersam, *Nano Lett.*, 2008, **8**, 1417–1422.

142 J. A. Fagan, M. L. Becker, J. Chun and E. K. Hobbie, *Adv. Mater.*, 2008, **20**, 1609–1613.
143 R. M. Jain, R. Howden, K. Tvrdy, S. Shimizu, A. J. Hilmer, T. P. McNicholas, K. K. Gleason and M. S. Strano, *Adv. Mater.*, 2012, **24**, 4436–4439.
144 T. Hertel, V. Perebeinos, J. Crochet, K. Arnold, M. Kappes and P. Avouris, *Nano Lett.*, 2008, **8**, 87–91.
145 C. Manzoni, A. Gambetta, E. Menna, M. Meneghetti, G. Lanzani and G. Cerullo, *Phys. Rev. Lett.*, 2005, **94**, 207401.
146 S. Berciaud, L. Cognet and B. Lounis, *Phys. Rev. Lett.*, 2008, **101**, 077402.
147 S. Cambré, S. M. Santos, W. Wenseleers, A. R. T. Nugraha, R. Saito, L. Cognet and B. Lounis, *ACS Nano*, 2012, **6**, 2649–2655.
148 T. Gokus, L. Cognet, J. G. Duque, M. Pasquali, A. Hartschuh and B. Lounis, *J. Phys. Chem. C*, 2010, **114**, 14025–14028.
149 J. J. Crochet, J. G. Duque, J. H. Werner and S. K. Doorn, *Nat. Nanotechnol.*, 2012, **7**, 126–132.
150 J. Xie, T. Inaba, R. Sugiyama and Y. Homma, *Phys. Rev. B: Condens. Matter Mater. Phys.*, 2012, **85**, 085434.
151 V. M. Agranovich and Y. V. Konobeev, *Phys. Status Solidi B*, 1968, **27**, 435–442.
152 M. Engel, J. P. Small, M. Steiner, M. Freitag, A. A. Green, M. C. Hersam and P. Avouris, *ACS Nano*, 2008, **2**, 2445–2452.
153 T. Ogawa and T. Takagahara, *Phys. Rev. B: Condens. Matter Mater. Phys.*, 1991, **44**, 8138–8156.
154 E. H. Haroz, S. M. Bachilo, R. B. Weisman and S. K. Doorn, *Phys. Rev. B: Condens. Matter Mater. Phys.*, 2008, **77**, 125405.
155 K. F. Mak, J. Shan and T. F. Heinz, *Phys. Rev. Lett.*, 2011, **106**, 046401.
156 V. Perebeinos and P. Avouris, *Nano Lett.*, 2007, **7**, 609–613.
157 G. Weiser, *Phys. Rev. B: Condens. Matter Mater. Phys.*, 1992, **45**, 14076–14085.
158 A. D. Mohite, P. Gopinath, H. M. Shah and B. W. Alphenaar, *Nano Lett.*, 2007, **8**, 142–146.
159 M. Kasha, *Radiat. Res.*, 1963, **20**, 55–71.
160 C. Y. Wong, C. Curutchet, S. Tretiak and G. D. Scholes, *J. Chem. Phys.*, 2009, **130**, 081104.
161 M. Rohlfing, *Phys. Rev. Lett.*, 2012, **108**, 087402.
162 T. Brixner, J. Stenger, H. Vaswani, M. Cho, R. Blankenship and G. Fleming, *Nature*, 2005, **434**, 625–628.
163 M. Freitag, Y. Martin, J. A. Misewich, R. Martel and P. Avouris, *Nano Lett.*, 2003, **3**, 1067–1071.
164 N. M. Gabor, Z. Zhong, K. Bosnick, J. Park and P. L. McEuen, *Science*, 2009, **325**, 1367–1371.
165 T. DeBorde, J. Kevek, T. Sharf, J. Wardini and E. Minot, Nanotechnology (IEEE-NANO), 2011 11th IEEE Conference on, 2011, pp. 382–386.
166 J. Svensson and E. E. B. Campbell, *J. Appl. Phys.*, 2011, **110**, 111101.
167 L. V. Keldysh, *Zh. Eksp. Teor. Fiz.*, 1958, **34**, 1138.
168 K. Bosnick, N. Gabor and P. McEuen, *Appl. Phys. Lett.*, 2006, **89**, 163121.
169 M. G. Littman, M. M. Kash and D. Kleppner, *Phys. Rev. Lett.*, 1978, **41**, 103–107.
170 A. Mohite, G. Sumanasekera, K. Hirahara, S. Bandow, S. Iijima and B. Alphenaar, *Chem. Phys. Lett.*, 2005, **412**, 190–194.
171 A. Mohite, S. Chakraborty, P. Gopinath, G. U. Sumanasekera and B. W. Alphenaar, *Appl. Phys. Lett.*, 2005, **86**, 061114.
172 A. Mohite, J.-T. Lin, G. Sumanasekera and B. W. Alphenaar, *Nano Lett.*, 2006, **6**, 1369–1373.
173 A. D. Mohite, T. S. Santos, J. S. Moodera and B. W. Alphenaar, *Nat. Nanotechnol.*, 2009, **4**, 425–429.
174 V. Perebeinos, J. Tersoff and P. Avouris, *Phys. Rev. Lett.*, 2004, **92**, 257402.
175 D. Moses, J. Wang, A. J. Heeger, N. Kirova and S. Brazovski, *Proc. Natl. Acad. Sci. U. S. A.*, 2001, **98**, 13496–13500.
176 T. Bansal, A. D. Mohite, H. M. Shah, C. Galande, A. Srivastava, J. B. Jasinski, P. M. Ajayan and B. W. Alphenaar, *Carbon*, 2012, **50**, 808–814.
177 H. M. Shah, A. D. Mohite, T. Bansal and B. W. Alphenaar, *Appl. Phys. Lett.*, 2010, **97**, 263301.
178 S. Vaddiraju, A. Mohite, A. Chin, M. Meyyappan, G. Sumanasekera, B. W. Alphenaar and M. K. Sunkara, *Nano Lett.*, 2005, **5**, 1625–1631.
179 Z. Wu, Z. Chen, X. Du, J. M. Logan, J. Sippel, M. Nikolou, K. Kamaras, J. R. Reynolds, D. B. Tanner, A. F. Hebard and A. G. Rinzler, *Science*, 2004, **305**, 1273–1276.
180 J. van de Lagemaat, T. M. Barnes, G. Rumbles, S. E. Shaheen, T. J. Coutts, C. Weeks, I. Levitsky, J. Peltola and P. Glatkowski, *Appl. Phys. Lett.*, 2006, **88**, 233503.
181 T. M. Barnes, X. Wu, J. Zhou, A. Duda, J. van de Lagemaat, T. J. Coutts, C. L. Weeks, D. A. Britz and P. Glatkowski, *Appl. Phys. Lett.*, 2007, **90**, 243503.
182 M. A. Contreras, T. Barnes, J. van de Lagemaat, G. Rumbles, T. J. Coutts, C. Weeks, P. Glatkowski, I. Levitsky, J. Peltola and D. A. Britz, *J. Phys. Chem. C*, 2007, **111**, 14045–14048.
183 J. L. Blackburn, T. M. Barnes, M. C. Beard, Y.-H. Kim, R. C. Tenent, T. J. McDonald, B. To, T. J. Coutts and M. J. Heben, *ACS Nano*, 2008, **2**, 1266–1274.
184 K. S. Mistry, B. A. Larsen, J. D. Bergeson, T. M. Barnes, G. Teeter, C. Engtrakul and J. L. Blackburn, *ACS Nano*, 2011, **5**, 3714–3723.
185 T. M. Barnes, J. L. Blackburn, J. van de Lagemaat, T. J. Coutts and M. J. Heben, *ACS Nano*, 2008, **2**, 1968–1976.
186 M. C. Beard, J. L. Blackburn and M. J. Heben, *Nano Lett.*, 2008, **8**, 4238–4242.
187 B. Chandra, A. Afzali, N. Khare, M. M. El-Ashry and G. S. Tulevski, *Chem. Mater.*, 2010, **22**, 5179–5183.
188 M. W. Rowell, M. A. Topinka, M. D. McGehee, H.-J. Prall, G. Dennler, N. S. Sariciftci, L. Hu and G. Gruner, *Appl. Phys. Lett.*, 2006, **88**, 233506.
189 T. M. Barnes, J. D. Bergeson, R. C. Tenent, B. A. Larsen, G. Teeter, K. M. Jones, J. L. Blackburn and J. van de Lagemaat, *Appl. Phys. Lett.*, 2010, **96**, 243309.
190 T. M. Barnes, M. O. Reese, J. D. Bergeson, B. A. Larsen, J. L. Blackburn, M. C. Beard, J. Bult and J. van de Lagemaat, *Adv. Energy Mater.*, 2012, **2**, 353–360.

191 A. J. Ferguson, J. L. Blackburn and N. Kopidakis, *Mater. Lett.*, 2013, **90**, 115–125.
192 A. J. Ferguson, J. L. Blackburn, J. M. Holt, N. Kopidakis, R. C. Tenent, T. M. Barnes, M. J. Heben and G. Rumbles, *J. Phys. Chem. Lett.*, 2010, **1**, 2406–2411.
193 H. W. Lee, Y. Yoon, S. Park, J. H. Oh, S. Hong, L. S. Liyanage, H. Wang, S. Morishita, N. Patil, Y. J. Park, J. J. Park, A. Spakowitz, G. Galli, F. Gygi, P. H. S. Wong, J. B. H. Tok, J. M. Kim and Z. Bao, *Nat. Commun.*, 2011, **2**, 541.
194 S. D. Stranks, C.-K. Yong, J. A. Alexander-Webber, C. Weisspfennig, M. B. Johnston, L. M. Herz and R. J. Nicholas, *ACS Nano*, 2012, **6**, 6058–6066.
195 S. D. Stranks, C. Weisspfennig, P. Parkinson, M. B. Johnston, L. M. Herz and R. J. Nicholas, *Nano Lett.*, 2011, **11**, 66–72.
196 M. Ichida, S. Mizuno, Y. Tani, Y. Saito and A. Nakamura, *J. Phys. Soc. Jpn.*, 1999, **68**, 3131–3133.
197 C. Sheng, Z. Vardeny, A. Dalton and R. Baughman, *Synth. Met.*, 2005, **155**, 254–257.
198 Z. Wang, H. Pedrosa, T. Krauss and L. Rothberg, *Phys. Rev. Lett.*, 2006, **96**, 047403.
199 S. Zaric, G. N. Ostojic, J. Shaver, J. Kono, O. Portugall, P. H. Frings, G. L. J. A. Rikken, M. Furis, S. A. Crooker, X. Wei, V. C. Moore, R. H. Hauge and R. E. Smalley, *Phys. Rev. Lett.*, 2006, **96**, 016406.
200 P. Avouris, M. Freitag and V. Perebeinos, *Nat. Photonics*, 2008, **2**, 341–350.
201 H. Huang, J. Marie, H. Kajiura and M. Ata, *Nano Lett.*, 2002, **2**, 1117–1119.
202 B. J. Landi, C. D. Cress, C. M. Evans and R. P. Raffaelle, *Chem. Mater.*, 2005, **17**, 6819–6834.
203 K. Yanagi, T. Okazaki, Y. Miyata and H. Kataura, *Chem. Phys. Lett.*, 2006, **431**, 145–148.
204 J. Yi, B. Aissa and M. El Khakani, *J. Nanosci. Nanotechnol.*, 2007, **7**, 3394–3399.
205 S. Lebedkin, I. Kareev, F. Hennrich and M. M. Kappes, *J. Phys. Chem. C*, 2008, **112**, 16236–16239.
206 J. U. Lee, *Appl. Phys. Lett.*, 2005, **87**, 073101.
207 C. Chen, W. Zhang, E. S.-W. Kong and Y. Zhang, *Appl. Phys. Lett.*, 2009, **94**, 263501.
208 S. Wang, L. Zhang, Z. Zhang, L. Ding, Q. Zeng, Z. Wang, X. Liang, M. Gao, J. Shen, H. Xu, Q. Chen, R. Cui, Y. Li and L.-M. Peng, *J. Phys. Chem. C*, 2009, **113**, 6891–6893.
209 G. Li, Y. Yao, H. Yang, V. Shrotriya, G. Yang and Y. Yang, *Adv. Funct. Mater.*, 2007, **17**, 1636–1644.
210 S. C. Price, A. C. Stuart, L. Yang, H. Zhou and W. You, *J. Am. Chem. Soc.*, 2011, **133**, 4625–4631.
211 H. Zhou, L. Yang, S. C. Price, K. J. Knight and W. You, *Angew. Chem., Int. Ed.*, 2010, **49**, 7992–7995.
212 M. P. Ramuz, M. Vosgueritchian, P. Wei, C. Wang, Y. Gao, Y. Wu, Y. Chen and Z. Bao, *ACS Nano*, 2012, **6**, 10384–10395.
213 C. Bounioux, E. A. Katz and R. Yerushalmi-Rozen, *Polym. Adv. Technol.*, 2012, **23**, 1129–1140.
214 S. Kazaoui, N. Minami, B. Nalini, Y. Kim and K. Hara, *J. Appl. Phys.*, 2005, **98**, 084314.
215 B. J. Landi, R. P. Raffaelle, S. L. Castro and S. G. Bailey, *Prog. Photovoltaics*, 2005, **13**, 165–172.
216 J. Lohrman, C. Zhang, W. Zhang and S. Ren, *Chem. Commun.*, 2012, **48**, 8377–8379.
217 V. C. Tung, J.-H. Huang, J. Kim, A. J. Smith, C.-W. Chu and J. Huang, *Energy Environ. Sci.*, 2012, **5**, 7810–7818.
218 V. C. Tung, J.-H. Huang, I. Tevis, F. Kim, J. Kim, C.-W. Chu, S. I. Stupp and J. Huang, *J. Am. Chem. Soc.*, 2011, **133**, 4940–4947.
219 M. Bernardi, J. Lohrman, P. V. Kumar, A. Kirkeminde, N. Ferralis, J. C. Grossman and S. Ren, *ACS Nano*, 2012, **6**, 8896–8903.
220 F. Wang, G. Dukovic, L. E. Brus and T. F. Heinz, *Phys. Rev. Lett.*, 2004, **92**, 177401.
221 A. Hagen, G. Moos, V. Talalaev and T. Hertel, *Appl. Phys. A: Mater. Sci. Process.*, 2004, **78**, 1137–1145.
222 Y.-Z. Ma, J. Stenger, J. Zimmermann, S. M. Bachilo, R. E. Smalley, R. B. Weisman and G. R. Fleming, *J. Chem. Phys.*, 2004, **120**, 3368–3373.
223 A. Hagen, M. Steiner, M. B. Raschke, C. Lienau, T. Hertel, H. Qian, A. J. Meixner and A. Hartschuh, *Phys. Rev. Lett.*, 2005, **95**, 197401.
224 Y.-Z. Ma, L. Valkunas, S. L. Dexheimer, S. M. Bachilo and G. R. Fleming, *Phys. Rev. Lett.*, 2005, **94**, 157402.
225 A. J. Siitonen, D. A. Tsyboulski, S. M. Bachilo and R. B. Weisman, *Nano Lett.*, 2010, **10**, 1595–1599.
226 S. Moritsubo, T. Murai, T. Shimada, Y. Murakami, S. Chiashi, S. Maruyama and Y. K. Kato, *Phys. Rev. Lett.*, 2010, **104**, 247402.
227 P. Peumans, A. Yakimov and S. R. Forrest, *J. Appl. Phys.*, 2003, **93**, 3693–3723.
228 D. E. Markov, E. Amsterdam, P. W. M. Blom, A. B. Sieval and J. C. Hummelen, *J. Phys. Chem. A*, 2005, **109**, 5266–5274.
229 S. R. Scully and M. D. McGehee, *J. Appl. Phys.*, 2006, **100**, 034907.
230 P. Heremans, D. Cheyns and B. P. Rand, *Acc. Chem. Res.*, 2009, **42**, 1740–1747.
231 R. R. Lunt, N. C. Giebink, A. A. Belak, J. B. Benziger and S. R. Forrest, *J. Appl. Phys.*, 2009, **105**, 053711.

